Elsevier Editorial System(tm) for BBA - Biomembranes
Manuscript Draft

Manuscript Number:

Title: HIV-1 Tat membrane interaction probed using X-ray and neutron scattering, CD spectroscopy and MD simulations

Article Type: Regular Paper

Keywords: Low-angle X-ray scattering (LAXS), wide-angle X-ray scattering (WAXS), circular dichroism spectroscopy, molecular dynamics (MD) simulations, lipid bilayer structure

Corresponding Author: Prof. Stephanie A. Tristram-Nagle, Ph.D.

Corresponding Author's Institution: Carnegie Mellon University

First Author: Kiyotaka Akabori

Order of Authors: Kiyotaka Akabori; Kun Huang; Bradley W Treece; Michael S Jablin; Brian B Maranville; Arthur R Woll; John F Nagle; Angel E Garcia; Stephanie A. Tristram-Nagle, Ph.D.

Abstract: We report the effect on lipid bilayers of the Tat peptide G48RKKRRQRRRPPQ60 from the HIV-1 virus transactivator of translation (Tat) protein. Synergistic use of low-angle X-ray scattering (LAXS) and atomistic molecular dynamics simulations (MD) indicate Tat peptide binding to neutral dioleoylphosphocholine (DOPC) lipid headgroups. This binding induced the local lipid phosphate groups to move 3 Å closer to the center of the bilayer. Many of the positively charged guanidinium components of the arginines were as close to the center of the bilayer as the locally thinned lipid phosphate groups. LAXS data for DOPC, DOPC/ dioleoylphosphoethanolamine (DOPE), DOPC/ dioleoylphosphoserine (DOPS), and a mimic of the nuclear membrane gave similar results. Generally, the Tat peptide decreased the bilayer bending modulus KC and increased the area/lipid. Further indications that Tat softens a membrane, thereby facilitating translocation, were provided by wide-angle X-ray scattering (WAXS) and neutron scattering. CD spectroscopy was also applied to further characterize Tat/membrane interactions. Although a mechanism for translation remains obscure, this study suggests that the peptide/lipid interaction makes the Tat peptide poised to translocate from the headgroup region.

Suggested Reviewers: Gerard Wong
gclwong@seas.ucla.edu
Dr. Wong has published many papers on peptide/lipid interactions, including Tat/membrane interactions.

Toby Allen
twallen@ucdavis.edu
Dr. Allen has carried out MD simulations of positively charged peptides in membranes, so he is very familiar with this system.

Peter Tieleman
tieleman@ucalgary.ca

Dr. Tieleman has carried out simulations of peptide/membrane interactions, so he will appreciate our contribution.

Jianjun Pan
panj@usf.edu
Dr. Pan is an expert in membrane structure so he will be capable of evaluating our work very well.

Carnegie Mellon University

Department of Physics
Carnegie Mellon University
Pittsburgh, Pennsylvania 15213-3890
(412) 268-2740
April 25, 2014

Dr. Yechiel Shai
BBA – Biomembranes

Dear Editor Shai:

We are submitting our interesting manuscript about HIV-1 Tat-membrane interactions. Our results were obtained with X-ray and neutron scattering, MD simulations, CD spectroscopy and volume measurements. Due to a past experience, I would like to request that Editor Robert Brasseur not be asked to handle this article. When Dr. Brasseur handled a previous manuscript that we submitted to BBA, there was a very lengthy review process. Any other editor of your choice would be appropriate.

Thank you for considering our manuscript as a regular article in BBA - Biomembranes. Best regards,

Dr. Stephanie Tristram-Nagle, Ph.D.
Research Professor

Dr. Stephanie Tristram-Nagle, Research Professor
Biological Physics Group, Physics Dept.
stn@cmu.edu 412-268-3174
http://www.cmu.edu/biophys/jfstn

Graphical Abstract (for review)

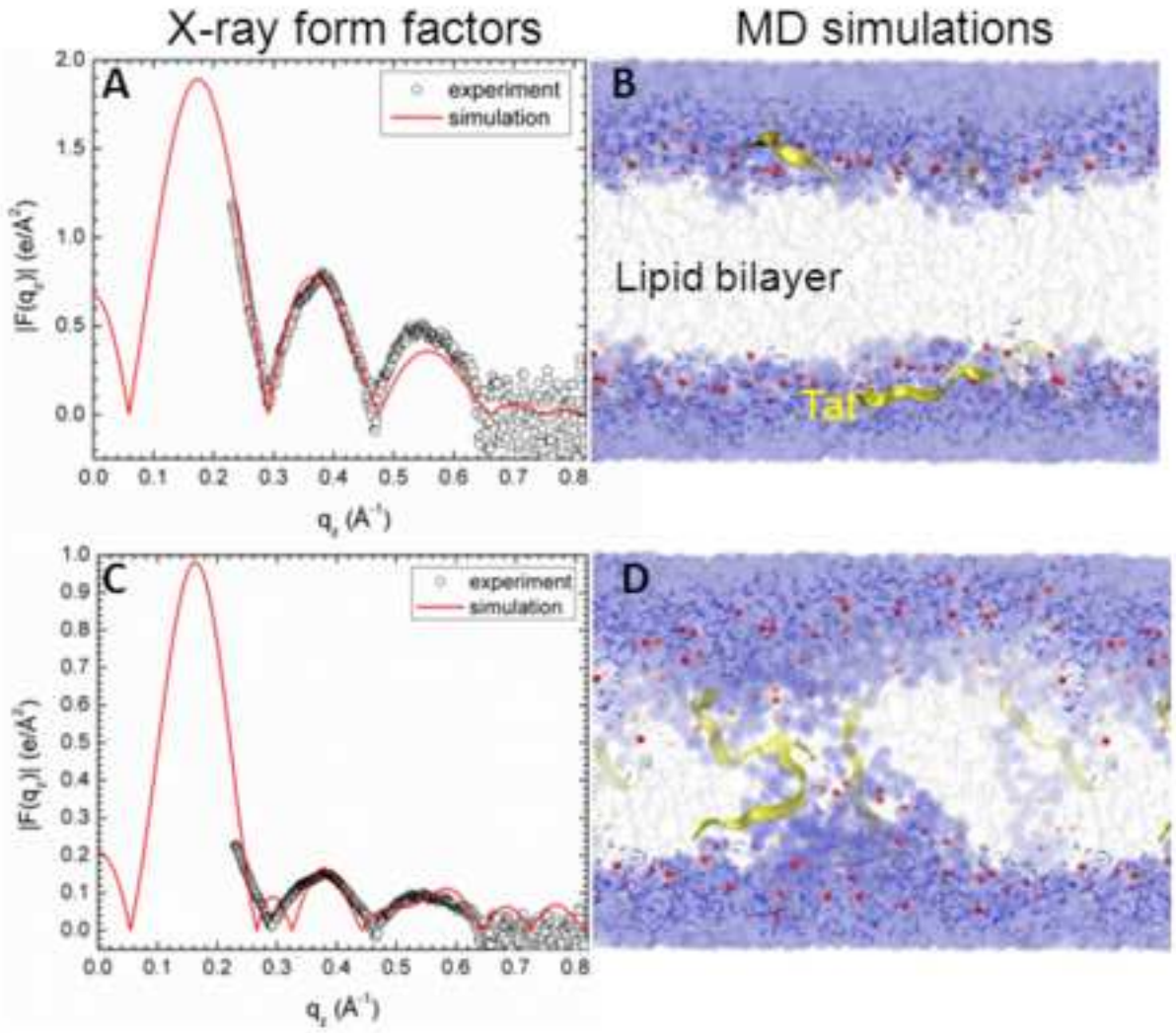

Highlights

- Tat causes ~1-2 Å average thinning of three membrane mimics
- Local thinning near Tat is ~3 Å determined by MD simulations of DOPC/Tat
- Tat increases area/lipid by ~3-5 $Å^2$ and softens membranes
- Tat decreases chain order and increases mosaic spread
- A water-filled pore formed by Tat is not supported by this study

HIV-1 Tat membrane interaction probed using X-ray and neutron scattering, CD spectroscopy and MD simulations

Kiyotaka Akabori[1], Kun Huang[2], Bradley W. Treece[1], Michael S. Jablin[1], Brian Maranville[3], Arthur Woll[4], John F. Nagle[1], Angel E. Garcia[2], and Stephanie Tristram-Nagle[1]

[1]Department of Physics, Carnegie Mellon University, 5000 Forbes Avenue, Pittsburgh, Pennsylvania, [2]Department of Physics, Rensselaer Polytechnic Institute, 110 Eighth Street, Troy, NY 12180, [3]NIST Center for Neutron Research, 100 Bureau Drive, Stop 6102, Gaithersburg, MD 20899, [4]CHESS, Cornell University, 161 Synchrotron Drive, Ithaca, NY 14853

Running Title: HIV Tat/membrane structure and properties

Keywords: Low-angle X-ray scattering (LAXS), wide-angle X-ray scattering (WAXS), circular dichroism spectroscopy, molecular dynamics (MD) simulations, lipid bilayer structure

4/9/2014

Abstract

We report the effect on lipid bilayers of the Tat peptide G_{48}RKKRRQRRRPPQ$_{60}$ from the HIV-1 virus transactivator of translation (Tat) protein. Synergistic use of low-angle X-ray scattering (LAXS) and atomistic molecular dynamics simulations (MD) indicate Tat peptide binding to neutral dioleoylphosphocholine (DOPC) lipid headgroups. This binding induced the local lipid phosphate groups to move 3 Å closer to the center of the bilayer. Many of the positively charged guanidinium components of the arginines were as close to the center of the bilayer as the locally thinned lipid phosphate groups. LAXS data for DOPC, DOPC/dioleoylphosphoethanolamine (DOPE), DOPC/dioleoylphosphoserine (DOPS), and a mimic of the nuclear membrane gave similar results. Generally, the Tat peptide decreased the bilayer bending modulus K_C and increased the area/lipid. Further indications that Tat softens a membrane, thereby facilitating translocation, were provided by wide-angle X-ray scattering (WAXS) and neutron scattering. CD spectroscopy was also applied to further characterize Tat/membrane interactions. Although a mechanism for translation remains obscure, this study suggests that the peptide/lipid interaction makes the Tat peptide poised to translocate from the headgroup region.

Abbreviations: dioleoylphosphocholine (DOPC), dioleoylphosphoethanolamine (DOPE), dioleoylphosphoserine (DOPS), palmitoyloleoylphosphocholine (POPC), palmitoyloleoylphosphoethanolamine (POPE), palmitoyloleoylphosphoserine (POPS), Soy phosphoinositol (Soy PI), sphingomyelin (SM), cholesterol (Chol), bis(monoacylglycerol)-phosphate) (BMP), phosphoglycerol (PG), cell-penetrating peptide (CPP), giant unilamellar vesicles (GUVs), large unilamellar vesicles (LUVs), low-angle X-ray scattering (LAXS), wide-angle X-ray scattering (WAXS), hexafluoroisopropanol (HFP), trifluoroethanol (TFE), Define Secondary Structure of Proteins (DSSP)

Keywords: cell-penetrating peptide, X-ray and neutron scattering, HIV-1 Tat, MD simulations, peptide translocation, membrane pore

1. Introduction

The name cell-penetrating peptide (CPP) connotes a peptide that easily penetrates cell membranes (for Reviews see [1-3]). The present work focuses on the transactivator of translation, Tat, from the HIV-1 virus, which plays a role in AIDS progression. Early work showed that the HIV-Tat transactivator protein (86 amino acids) was efficiently taken up by cells, and concentrations as low as 1 nM were sufficient to transactivate a reporter gene expressed from the HIV-1 promoter [4, 5]. It has been reported that Tat protein uptake does not require ATP [6]. Studies using inhibitors of different types of endocytosis, including clathrin- and caveolae-mediated, or receptor-independent macropinocytosis reached the same conclusion that ATP mediated endocytosis is not involved in Tat protein permeation [7-10]. However, this issue is controversial, as other studies found evidence for endocytosis in Tat protein import [11-19]. Still other studies have concluded that an ATP requirement for Tat protein entry depends on the size of the cargo attached to Tat protein, or on the specific cell type [20-22].

The part of the Tat protein responsible for cellular uptake was assigned to a short region Tat (48-60), G_{48}RKKRRQRRRPPQ$_{60}$, which is particularly rich in basic amino acids [6]. Deletion of three out of eight positive charges in this region caused loss of its ability to translocate [6]. In this manuscript short basic regions will be called Tat, while the entire 86-amino acid protein will be called Tat protein. Tat was shown to be responsible for the Tat protein's permeation into the cell nucleus and the nucleoli [6], and this was confirmed using live cell fluorescence in SVGA cells [23]. Tat (48-60) was shown to have little toxicity on HeLa cells at 100 μM concentration [6], but the longer Tat protein (2-86) was toxic to rat brain glioma cells at 1-10 μM [24]. Interestingly, no hemolytic activity was found when human erythrocytes were incubated with a highly neurotoxic concentration (40 μM) of Tat (2-86) [24]. These results prompt the question, what is the mechanism of Tat's translocation through membranes?

To address this question, many biophysical studies have used simple models of biological membranes composed of a small number of lipid types. These studies are valuable because there is no possibility for ATP-dependent translocation, thus ruling out endocytosis if translocation occurs. For example, Mishra et al. reported that the rate of entry into giant unilamellar vesicles (GUVs) composed of PS/PC (1:4 mole ratio) lipids of rhodamine-tagged Tat is immeasurably slow, but it crosses a GUV composed of PS/PC/PE (1:2:1) lipids within 30 seconds [25]. This study suggests that negative curvature induced by the inclusion of PE facilitates translocation. In a subsequent study using much smaller unilamellar vesicles (LUVs), Tat did not release an encapsulated fluorescent probe in LUVs composed of lipids modeling the outer plasma membrane, PC/PE/SM/Chol (1:1:1:1.5), but did release the probe in LUVs composed of BMP/PC/PE (77:19:4) [26]; BMP (bis(monoacylglycero)-phosphate) is an anionic lipid specific to late endosomes. In that study [26], the inclusion of PE did not suffice to cause leaky fusion in LUVs in the absence of a negatively charged lipid. The contrasting results in these two experiments may also be due to the use of LUVs instead of GUVs since it was reported that Tat does not translocate across LUVS of PC/PG (3:2) but does translocate across GUVs of the same lipid composition [27]. In a similar experiment, Tat did not translocate into egg PC LUVs [28]. In another experiment confirming these results, Tat did not translocate into GUVS containing only PC with 20 mol% cholesterol, but when PS or PE was included with PC, then rapid translocation of Tat was observed [29]. These experiments demonstrate that the choice of lipids and model systems influences Tat translocation.

Is a pore formed during Tat translocation? Although direct conductance measurements of Tat and lipid membranes have not been carried out, two studies measured conductance with the somewhat similar CPP oligoarginine R9C peptide. Using single-channel conductance of gramicidin A in planar lipid membranes consisting of anionic, neutral or positively charged lipids, R9C did not increase conductance, even in anionic lipid membranes [30]. By contrast, in a similar experiment using planar lipid membranes, a current was induced by R9C in PC/PG (3:1) membranes, with increasing destabilization over time [31]. Thus questions remain about pore formation of Tat in membranes. In the GUV experiment with Tat mentioned above [29], Ciobanasu et al., using size exclusion methods, suggested a pore in the nanometer range, which could only be passed by small dye tracer molecules. Thus, if a true pore forms, it is likely to be small and transitory.

What is the secondary structure of Tat in membranes? Circular dichroism (CD) spectroscopy was carried out on, where the penultimate proline on Tat (48-60) was replaced by a tryptophan [27]. That study found a random coil secondary structure in aqueous solution as well as when mixed with PC/PG/PE (65:35:5) LUVs. The same result was obtained using CD in PC/PG (3:1) vesicles by Ziegler et al.[10], indicating that an alpha helix is not required for Tat's translocation ability. In addition, solid state NMR has identified a random coil structure of Tat in DMPC/DMPG (8:7 mole ratio) multibilayers [32]. In the larger Tat-(1-72)-protein NMR measurements at pH 4 have determined there is no secondary structure, with a dynamical basic region [33]. Similarly, NMR was used to study the full Tat protein and found a highly flexible basic region [34].

Regarding the mechanism of translocation of this randomly structured, short basic peptide, many models have been proposed based on the conflicting results listed above. Molecular dynamics simulations offer some insight into the molecular details of translocation. Herce and Garcia simulated the translocation of Tat (Y_{47}GRKKRRQRRR$_{57}$) across DOPC at various lipid:peptide molar ratios [35]. Their simulations indicated that Tat binds to the phosphate headgroups, with 1 Tat binding with 14 lipids, each positive charge on Tat-associated with nearly 2 phosphate groups [35]. Translocation involved a localized thinning, and snorkeling of arginine side chains through the hydrophobic layer to interact with phosphates on the other side of the membrane. This allowed some water molecules to penetrate the membrane along with Tat, forming a pore [35]. In this simulation, performed without inclusion of counterions, pore formation was only observed at high ratios of peptide:lipid (1:18) or at elevated temperature. However, a subsequent Gromacs simulation with counterions found no thinning and no pore formation when Tat was added to DOPC membranes [36]. Instead it found a membrane invagination associated with a cluster of Tat peptides, suggesting that micropinocytosis could be the model for Tat translocation across membranes [36].

In this work we primarily combine experimental low-angle X-ray scattering (LAXS) data with MD simulations to obtain the structure of fully hydrated, oriented lipid bilayers with Tat (47-57) added at several mole ratios. The lipid systems were DOPC, DOPC/DOPE (3:1 mole ratio), DOPC/DOPS (3:1), DOPC/DOPE (1:1) and a mimic of the nuclear membrane (POPC/POPE/POPS/SoyPI/Chol, 69:15:2:4:11). Accessory techniques, densitometry, wide-angle X-ray scattering (WAXS), neutron scattering, CD spectroscopy were also applied to further characterize Tat/membrane interactions.

2. Materials and methods

2.1 Lipids and peptides

Synthesized lipids were purchased from Avanti Polar Lipids (Alabaster, AL) and used without further purification. Membrane mimics were prepared by first dissolving lyophilized lipids in chloroform and then mixing these stock solutions to create the lipid compositions DOPC, DOPC/DOPE (3:1), DOPC/DOPE (1:1), DOPC/DOPS (3:1) and nuclear membrane mimic (POPC/POPE/POPS/SoyPI/Cholesterol, 69:15:2:4:11) (based on Ref. [37]). Peptide (Y_{47}GRKKRRQRRR$_{57}$) was purchased in two separate lots from the Peptide Synthesis Facility (University of Pittsburgh, Pittsburgh, PA); mass spectroscopy revealed >95% purity. This Tat peptide corresponds to residues (47-57) of the 86 residues in the Tat protein [6]. Tat was dissolved in HPLC trifluoroethanol (TFE) and then mixed with lipid stock solutions in chloroform to form mole fractions between 0.0044 and 0.108. Weight of Tat in these mole fractions was corrected for protein content (the remainder being 8 trifluoroacetate counter-ions from the peptide synthesis). Solvents were removed by evaporation in the fume hood followed by 2 hours in a vacuum chamber at room temperature.

2.2 Samples for X-ray and neutron scattering

Four mg dried lipid/peptide mixture was re-dissolved in HPLC chloroform/TFE (2:1 v:v) for most of the lipid compositions. However, DOPC/DOPS (3:1) mixtures required chloroform/HFP (1:1 v:v) in order to solubilize the negatively charged DOPS. 200 µl of 4 mg mixtures in solvents were plated onto silicon wafers (15x30x1 mm) via the rock and roll method [38] to produce stacks of ~1800 well-aligned bilayers; solvents were removed by evaporation in the fume hood, followed by two hours under vacuum. Samples were prehydrated through the vapor in polypropylene hydration chambers at 37^{o}C for 2-6 h directly before hydrating in the thick-walled X-ray hydration chamber [39] for 0.5–1 h. Pre-equilibration allowed sufficient time for equilibrium binding of peptides with membrane mimics.

2.3 Samples for densimetry

Multilamellar vesicles (MLVs) were prepared by mixing dried lipid mixtures with MilliQ water to a final concentration of 2-5 wt% in nalgene vials and cycling three times between -20^{o}C and 60^{o}C for ten minutes at each temperature with vortexing. Pure Tat was dissolved in water at 0.4 wt%.

2.4 Samples for circular dichroism (CD)

Thin films were prepared by spreading ~1 mg, x=0.11 (Peptide/(Lipid+Peptide)), in chloroform/TFE (1:1) onto one inside face of a quartz cuvette (Fisher Scientific, Pittsburgh, PA) and solvents were removed under vacuum. Our samples were purposely misoriented during spreading onto the cuvette side to minimize orientation effects on CD spectra [40, 41]. Hydration occurred through the vapor in sealed cuvettes at room temperature for 24 h. In addition, lyophilized Tat was also dissolved in 3 ml water (0.067 mg/ml) with no lipid.

2.5 X-ray scattering methods

LAXS. Low-angle X-ray scattering data from oriented fluid phase lipid mixtures at 37 ^{o}C were obtained at the Cornell High Energy Synchrotron Source (CHESS) using previously described methods [42, 43]. The analysis of diffuse LAXS from oriented stacks of fluctuating

fluid bilayers has been previously described [39]. Absolute form factors $|F(q_z)|$ were obtained as previously described [42]. Modeling to estimate the locations of Tat and the lipid components was performed using the SDP program [44].

WAXS. As described previously [45, 46], wide-angle X-ray scattering (WAXS) was obtained at a fixed angle of 0.5^o, background collected at -0.5^o was subtracted, and these data were analyzed to obtain the S_{xray} order parameter. Further details can be found in Supplementary data near **Fig. S4.**

2.6 Densimetry

Volumes of lipid mixtures with and without peptides in fully hydrated multilamellar vesicles (MLV) were determined at 37±0.01 ^oC using an Anton-Paar USA DMA5000M (Ashland, VA) vibrating tube densimeter [47].

2.7 CD spectroscopy

CD spectroscopy was carried out as described in Ref. [48]. Additional details and results can be found near **Fig. S5.**

2.8 Molecular dynamics simulations

Systems with different DOPC/Tat mole ratios (128:0, 128:2 and 128:4, corresponding to 0, 0.015 and 0.030 mole fractions) were simulated atomistically using the Gromacs 4.6.1 package [49]. DOPC was modeled by the Slipid force field [50, 51] and HIV Tat was modeled by Amber 99SB [52]. Tip3p water was used [53]. The number of Tats was divided equally on each side of the bilayer to mimic experimental conditions. All systems were simulated at 310 K with a constant area in the x-y plane for and 1 atm constant pressure in the Z direction. Each system was simulated for 100 ns and the last 50 ns was used as the production run.

At each DOPC/Tat mole ratio, we studied systems with three different area/lipid (A_L). For the DOPC system, we fixed A_L = 68, 70, 72 Å2; DOPC/Tat (128:2), we fixed the A_L = 72, 74, 76 $Å^2$; DOPC/Tat (128:4), we fixed the A_L =72, 74, 76 Å. For each DOPC/Tat system at fixed A_L, we then conducted seven independent simulations with the center of mass (COM) of each Tat constrained at different bilayer depths from the bilayer center (18, 16, 14, 12, 10, 8 and 5 Å). In total, 45 independent simulations were conducted. The goal of constrained simulations is to find the best match between experimental and MD simulation form factors. Comparison to the X-ray form factors was performed using the SIMtoEXP software [54]. Additional details concerning the MD simulations are in **Supplementary Data 6**.

2.9 Neutron scattering methods

Grazing angle of incidence neutron scattering data were obtained at the MAGIK beamline at the NIST Center for Neutron Research in Gaithersburg, Maryland using a hydration chamber designed by Drs. Tristram-Nagle and Frank Heinrich. The chamber is able to fully hydrate the horizontally-held oriented lipid bilayers, by heating a small well containing D_2O or H_2O, and by cooling the samples relative to the humid vapor using two Peltier coolers. More details concerning the sample chamber can be found at http://www.humidity.frank-heinrich.net/. Although the chamber can hold up to 10 silicon wafers, each containing ~2000 bilayers, most scans were collected with a 3 mm vertical slit on the samples, so that only three wafers

contributed to the scattering. The data were collected both out-of-plane (q_z) to observe the first order lamellar D-spacing, and in-plane (q_r) using a Denex 2D detector.

3. Results

3.1 Low-angle X-ray scattering (LAXS)

Fig. 1 shows the scattering intensity pattern from DOPC/DOPE (1:1) with mole fraction x=0.034 Tat. The diffuse lobes are due to equilibrium fluctuations that occur in these fully hydrated, oriented lipid/peptide samples. The intensity I(**q**) in the diffuse patterns provide the absolute values of the form factors $F(q_z)$, which are the Fourier transforms of the electron density profile, through the relation $I(\mathbf{q})=S(\mathbf{q})|F(q_z)|^2/q_z$, where $\mathbf{q}=(q_r,q_z)$, S(**q**) is the structure interference factor, and q_z^{-1} is the usual LAXS approximation to the Lorentz factor [39, 55, 56]. The first step in the analysis takes advantage of the q_r dependence of the scattering to obtain the bending modulus K_C with results shown in **Fig. 2**. As positively charged Tat concentration was increased, the lamellar repeat spacing D generally increased in neutral lipid bilayers and decreased in negatively charged bilayers, consistent with changes in electrostatic repulsive interactions. With few exceptions, the water space between bilayers exceeded 20 Å.

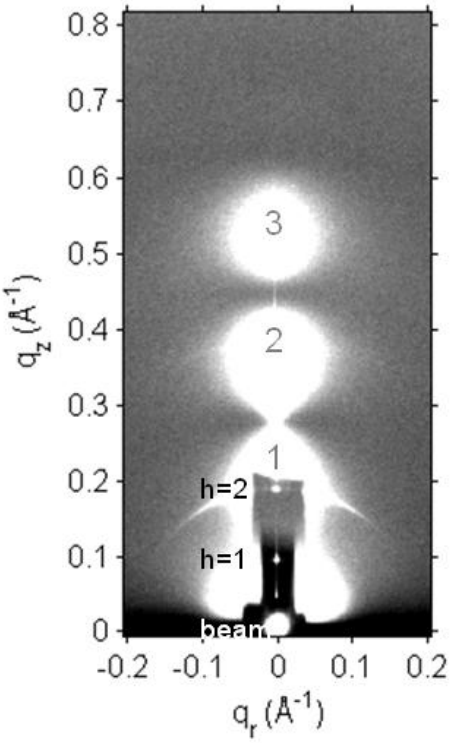

Figure 1. LAXS of DOPC/DOPE (1:1), x=0.034 Tat mole fraction (peptide/(lipid+peptide)) at 37 ^{o}C. White lobes of diffuse scattering intensity have large grey numbers, while lamellar orders and beam are shown to the left of the Molybdenum beam attenuator (short, dark rectangle). q_z and q_r are the projections of **q** along the direction normal and parallel to the membranes, respectively. The lamellar repeat spacing was D=66.2 Å.

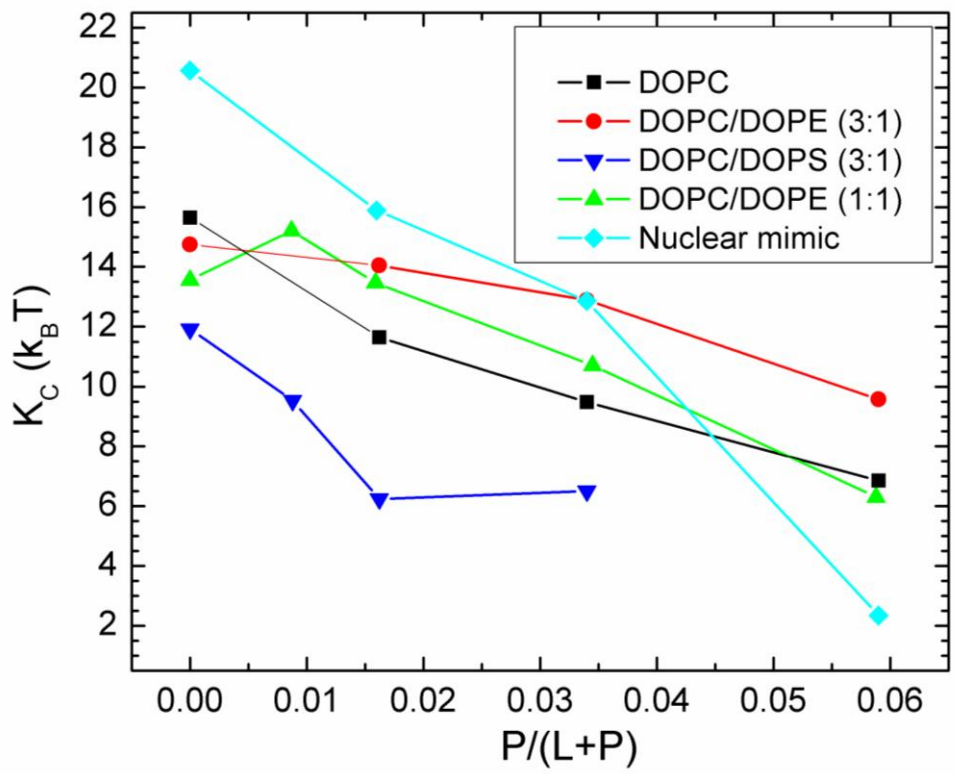

Figure 2. Bilayer bending modulus, K_C, vs. P/(L+P) mole fraction. D-spacings for DOPC/Tat mixtures varied from 64 to 68 Å, for DOPC/DOPE/Tat mixtures from 64 to 69 Å, for DOPC/DOPS/Tat (3:1) mixtures from 57 Å to >100 Å (pure DOPS was unbound), and for nuclear mimic/Tat mixtures from unbound (nuclear mimic) to 64 Å. Estimated uncertainty in all values is ± 2.

The analysis that obtains K_C also obtains the structure factor S(**q**) and then the unsigned form factors $|F(q_z)|$ are obtained from the intensity I(**q**) by division. Results for five different membrane mimics are shown in **Fig. 3.** Vertical lines indicate the "zero" position between the lobes of diffuse data where $F(q_z)$ change sign. In every sample, the zero positions shift to larger q_z, indicating a thinning of the membranes.

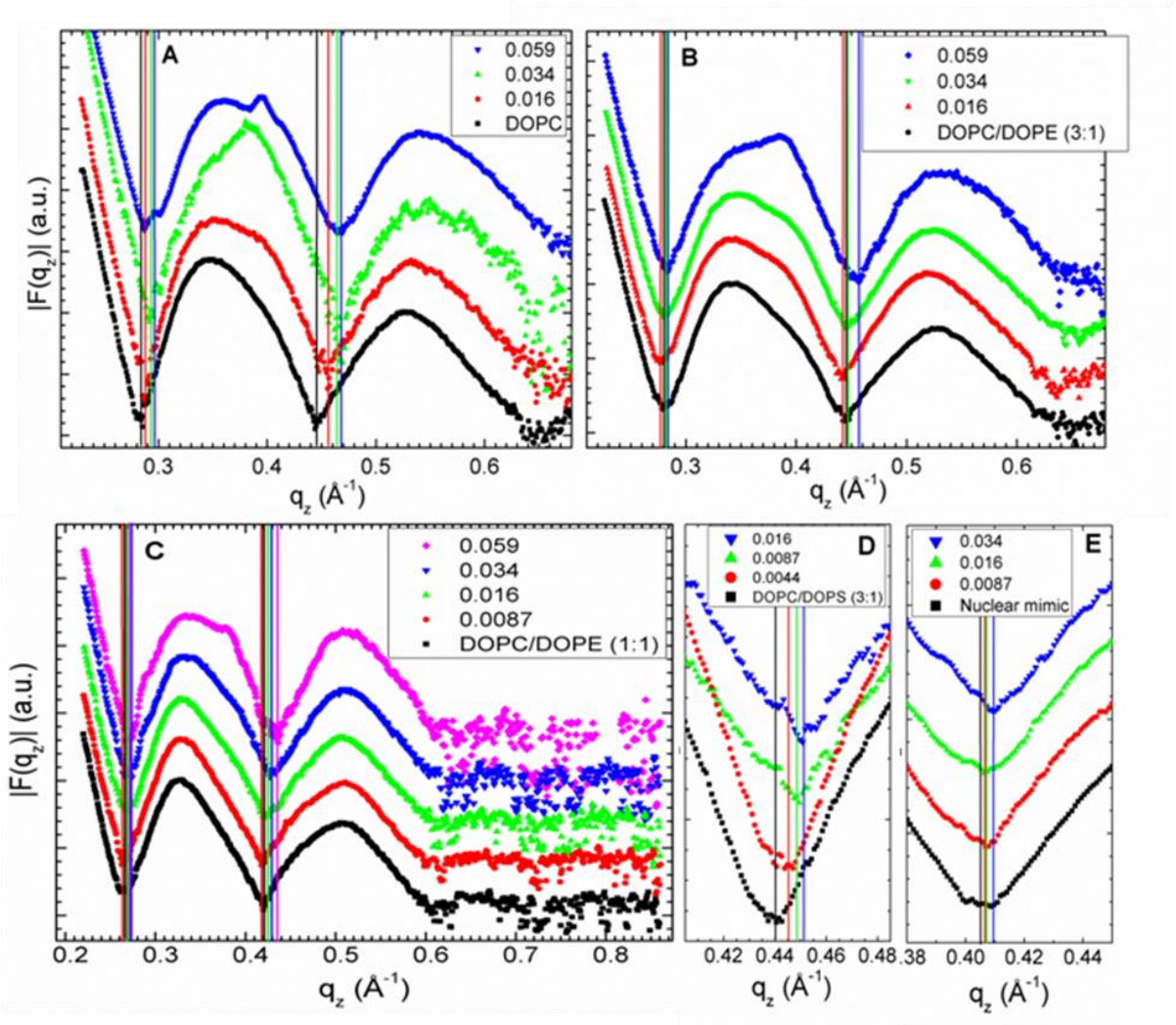

Figure 3. Form factors of lipid mixtures (arbitrarily scaled and vertically displaced) with increasing Tat mole fractions, P/(L+P), indicated on figure legends. Lipid mixtures: **A.** DOPC **B**. DOPC/DOPE (3:1) **C.** DOPC/DOPE (1:1) **D.** DOPC/DOPS (3:1) **E.** Nuclear mimic. The entire q_z range is shown in **C**, while others show partial ranges. Solid vertical lines indicate the q_z values where the form factors equal zero between the lobes of diffuse data.

3.2 MD simulations

Due to the slow relaxation in lipid bilayers and limited accuracy of the force field, a good agreement between experimental and MD simulation calculated form factors may be difficult to reach. Consequently, we carried out several constrained simulations at A_L and Z_{Tat} as described in Materials and Methods. We then compared the simulated form factor $F(q_z)$ with the experiment. The best match for DOPC/Tat (128:4) was found when the Tats were constrained at

18 Å away from the bilayer center (**Fig. 4.A,B**). The other best fit results were: DOPC A_L = 70 $Å^2$ and DOPC/Tat(128:2) A_L = 72 $Å^2$, Z_{Tat} = 18 Å. It clearly indicates that with increasing Tat concentration, A_L increases. The agreement worsened as Tat was constrained to be closer to the center of the bilayer. When Tats were constrained at 5 Å away from the bilayer center, we observed a spontaneous formation of water pores in the MD simulation. However, as shown in **Fig. 4.C** the corresponding form factor calculated from MD simulations does not match well with experiments.

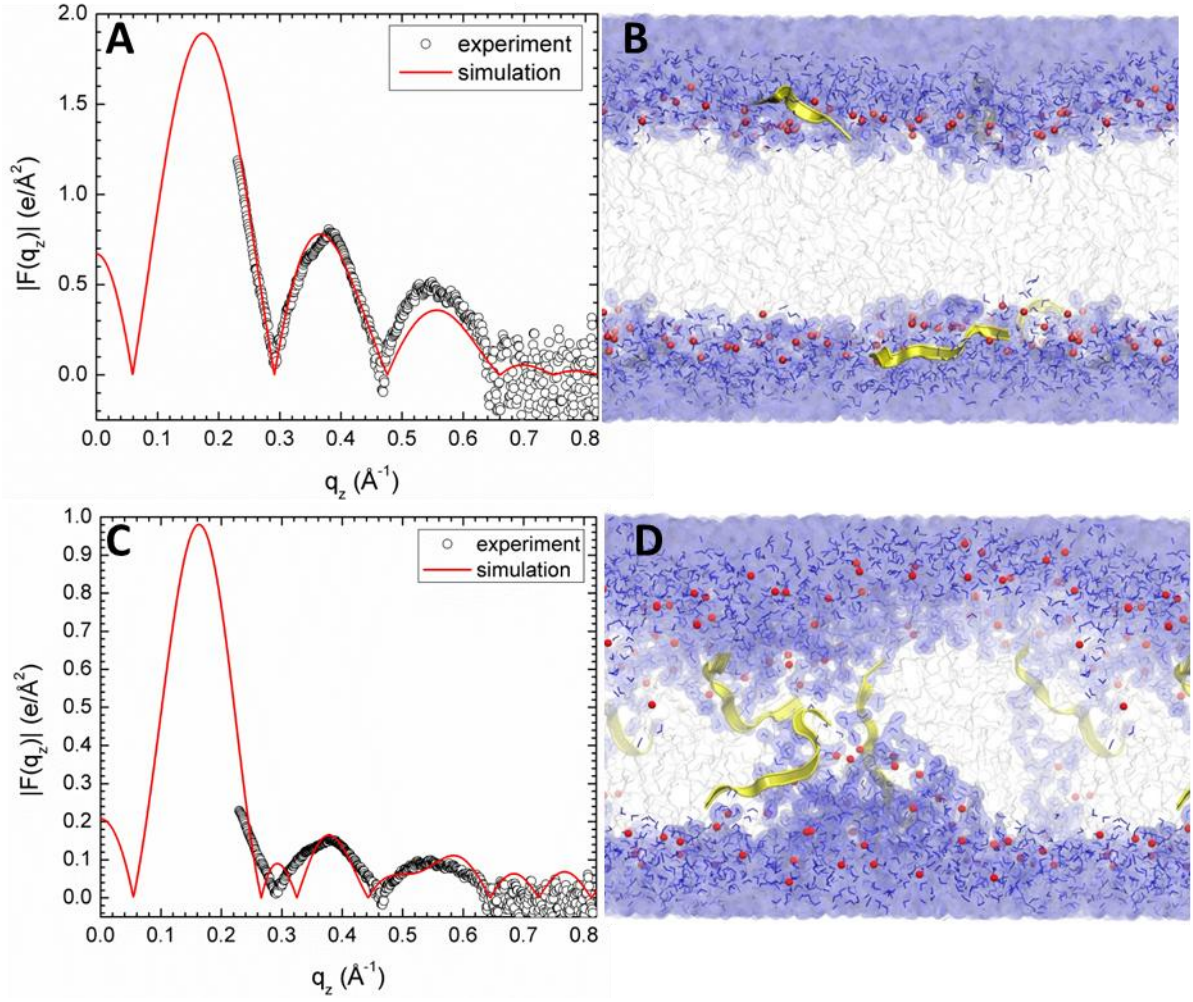

Figure 4. MD simulated form factors (red solid lines in **A** and **C)** of Tat/(DOPC+Tat), x=0.030, with Tat fixed at Z_{Tat}= 18 Å (panel **A**) and 5 Å (panel **C**) from the bilayer center compared to experimental form factors (open circles) scaled vertically to provide the best fit to the simulations. Corresponding snapshots are shown in Panels **B** and **D** in which the lipid chains are represented as grey sticks on a white background, Tats are yellow, phosphate groups are red and water is blue.

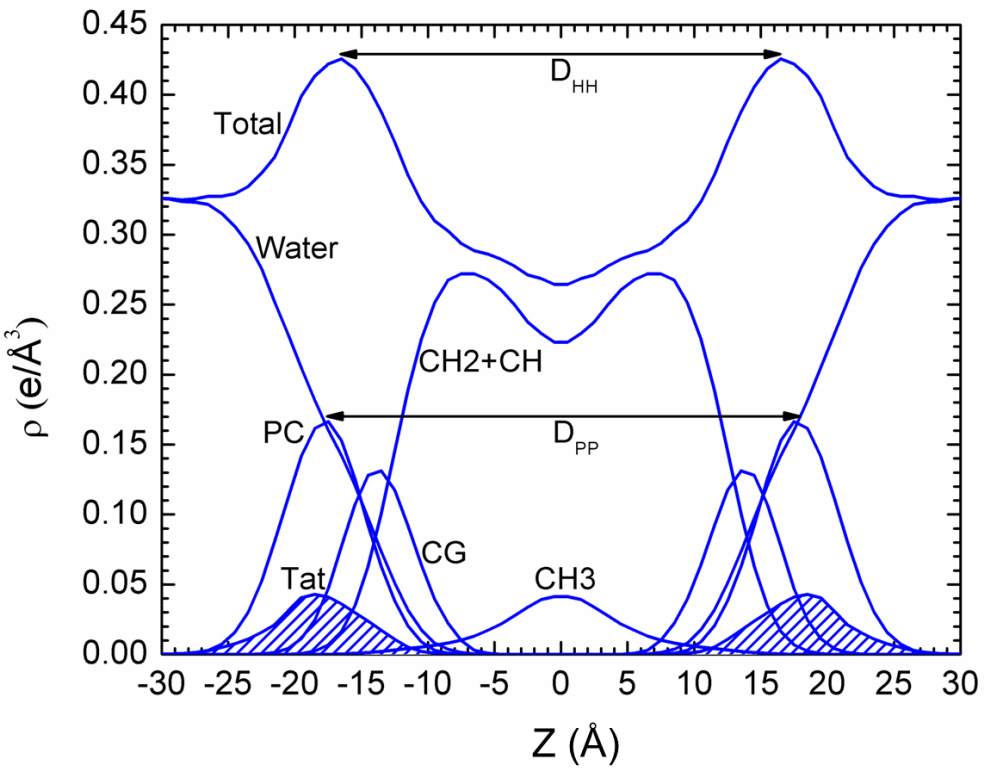

Figure 5. Symmetrized total electron density profile (EDP) from the simulation with the form factor shown in **Fig. 4A**. Also shown are the component group contributions. Component groups are labeled: PC, phosphocholine; CG, carbonyl-glycerol; CH2+CH, methylene and methine hydrocarbon region; CH3, terminal methyl; Tat peptide distribution is shaded.

3.3 SDP Modeling

We also estimate structure by fitting the experimental form factors using the SDP method [44] with the component groups identified in **Fig. 5**. The positions of these groups were free parameters and the agreement with the experimental form factors was excellent. Absolute total electron density profiles and the Tat profiles are shown for many samples in **Fig. 6 (A-C).** It must be emphasized, however, that, while the total EDP is well determined by this fitting procedure, the values of the parameters for the components are not as well determined as they would be if one had X-ray data to smaller and larger q_z and neutron data. Indeed, there are local minima in the fitting landscape, including one with Tat closer to the center of the bilayer as shown in **Fig. S5**. The simulations help to discard that result. For the results shown in **Fig. 6**, a consistent trend is that Tat moves away from the bilayer center as concentration increases. Electron density profiles for DOPC/DOPS (3:1) and the nuclear membrane mimic were not successful, due to loss of diffuse scattering by Tat's charge neutralization of these negatively charged membranes.

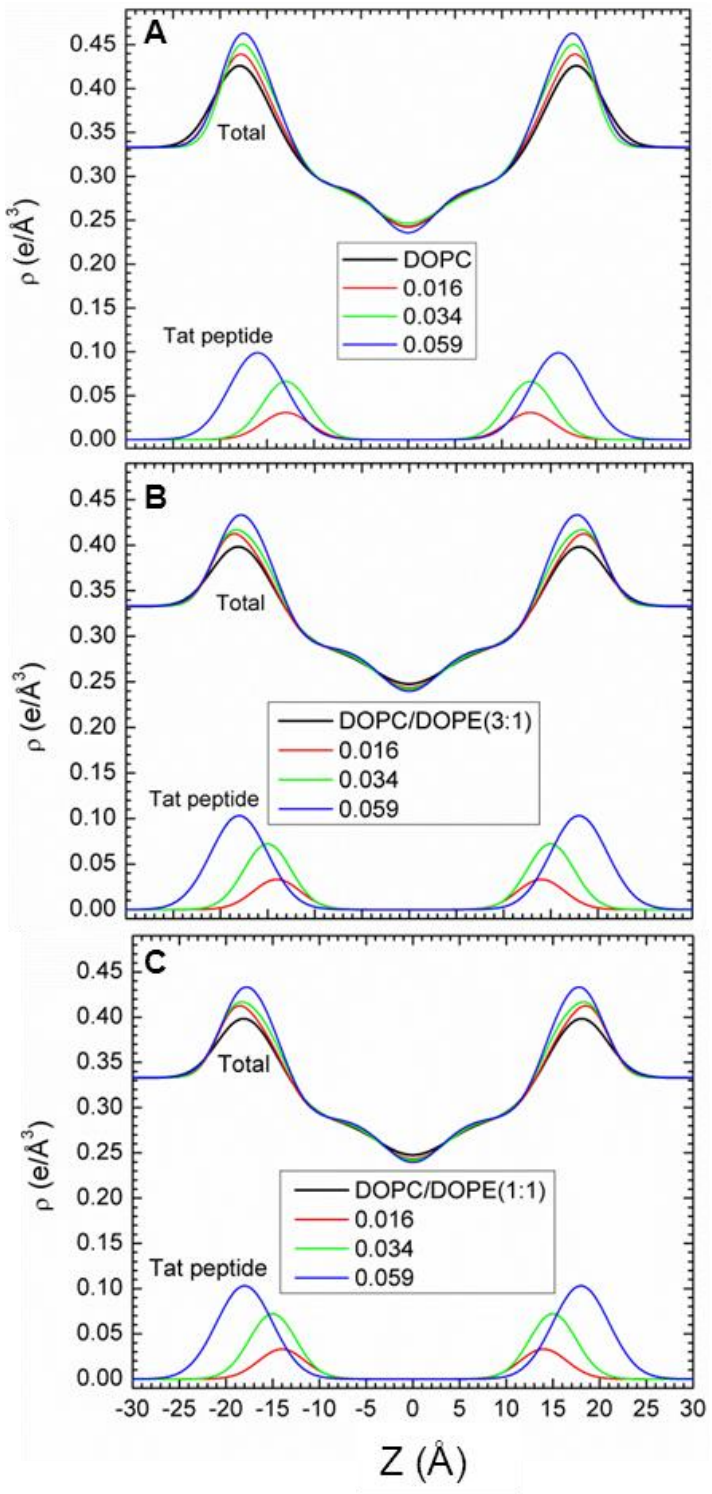

Figure 6. SDP modeling results for absolute electron density profiles (EDPs) and for the Tat location as a function of distance Z along the bilayer normal. **A.** DOPC **B.** DOPC/DOPE (3:1) and **C.** DOPC/DOPE (1:1).

More structural detail from the modeling and from the simulations is shown in **Fig. 7**. The bilayer thickness can be described as D_{HH}, which is the distance between the maxima in the electron density profile, or as D_{PP}, which is the distance between the phosphocholines on the opposing monolayers (see **Fig. 5**). **Figs. 7A** and **7B** show that both these quantities tend to decrease with increasing Tat mole fraction (P/(L+P)), showing that Tat thins membranes, increasingly so as its concentration is increased, even though both simulation and modeling suggest that Tat moves further from the membrane center with increasing concentration as shown in **Fig. 7D.** **Fig. 7C** shows that the area per lipid A_L usually increases with increasing mole fraction of Tat, similar to the findings from MD simulations (Section *3.2*), as would be expected. The results from the simulation data plotted in **Fig. 7** were obtained by using a weighted average based on chi-square of the four best fits of the simulated form factors with the experimental form factors.

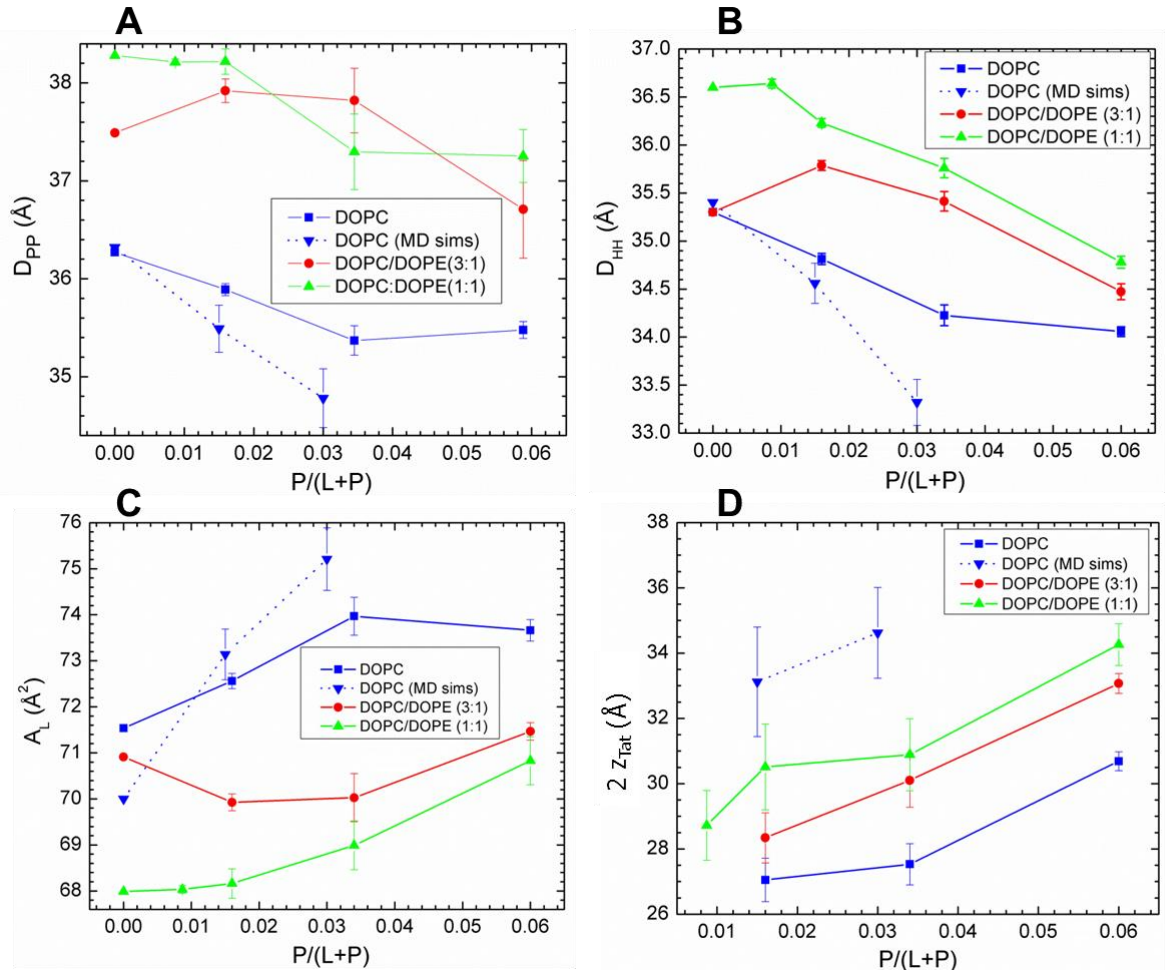

Figure 7. **A.** Bilayer thickness, D_{PP}; **B.** Bilayer thickness, D_{HH}; **C.** Area/lipid, A_L; **D.** Twice the Tat location, $2A_{Tat}$: all plotted vs. Tat mole fraction P/(L+P). Error bars are standard deviations from imposing Tat Gaussian widths, σ = 2.5, 3.0 or 3.5 Å. Inverted blue triangles connected with dotted line are results from MD simulations, averaging the best fits to the X-ray data for each parameter, with standard deviations shown.

3.4 S_{xray} order parameter from WAXS

Fig. 8 shows that the S_{xray} orientational order parameter generally decreases with increasing concentration of Tat for most of the membrane mimics studied. These decreases in membrane chain order are compatible with the increase in softening of membranes by Tat observed by a decrease in K_C in **Fig. 2**.

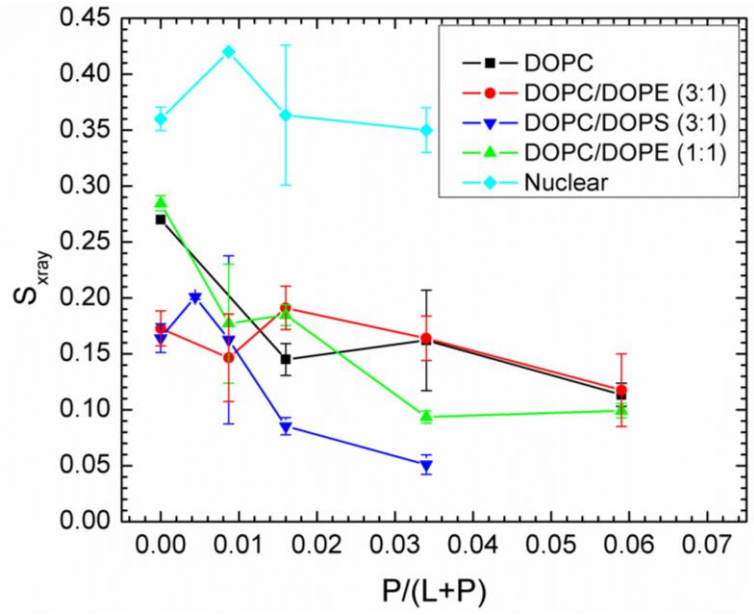

Figure 8. S_{xray}, orientational order parameter, vs. x=P/(L+P) mole fraction. Error bars are standard deviations determined by analyzing WAXS data from several lateral positions on the same sample.

3.5 CD spectroscopy

Results of the secondary structure of Tat determined using CD spectroscopy are shown in **Fig. S7** and details are given in the Supplementary data text. Basically, there was no effect of the DOPC/DOPE (3:1) membrane on the secondary structure of Tat (x=0.108) compared to Tat solubilized in water. The structure was primarily β and random coil, with <10% α-helix in both environments. The β structures include regular and distorted β-strands and β-turns. These results are summarized in **Table 1**.

Table 1. CD results

Sample	**α-Helix**	**β-Structures**	**Random Coil**
Tat in Water	0.061±0.016	0.574±0.049	0.363±0.038
Tat in Lipid Film	0.047±0.040	0.57±0.071	0.381±0.073

3.6 Volume results

Experimental and simulated volumes are given in **Table 2**. The simulated volume was obtained using the volume app in the SIMtoEXP program. The experimental Tat volume was calculated from the measured density assuming that the lipid volume was the same as with no Tat. In general, there may be an interaction volume between the peptide and the lipid membrane as we found previously for bacteriorhodopsin [57]. As lipid was present in excess to Tat, the partial molecular volume of the lipid should be the same as with no Tat, so this way of calculating includes all the interaction volume in V_{Tat}. Comparison of V_{Tat} in water with the result for 5:1 Lipid:Tat suggests that the interaction volume may be negative, consistent with a net attractive interaction with lipid. Understandably, values of V_{Tat} were unreliable for small mole ratios of Tat:Lipid. Therefore we used simple additivity for those mimics not shown in **Table 2** for the volumes used in the SDP program. All volumes obtained from the Gromacs MD simulations were somewhat smaller than the measured volumes, but it supports the Tat volume being closer to 1822 $Å^3$ than the outlying values obtained experimentally at small Tat concentrations.

Table 2. Volume results at 37 ^oC

Tat in:	**V_{lipid} ($Å^3$)**	**Lipid:Tat**	**V_{Tat} ($Å^3$)**
Water			1877
DOPC/DOPE (3:1)	1288	5:1	1822
DOPC	1314	39.6:1	676
DOPC/DOPS (3:1)	1298	39.6:1	2613
Simulations			
DOPC	1283	128:2	1694
DOPC	1294	128:4	1699

3.7 Summary of Results

We summarize our results for how Tat affects the lipid bilayer in **Fig. 9**. The height of Tat, H_{Tat} = 8.7 Å, was the full width at half maximum of the Tat electron density profiles obtained from simulations and the cylindrical radius, R_{Tat} = 8.3 Å, was calculated to give the measured volume. The Z distances from the center of the bilayer were derived from weighted averages of four MD simulations of Tat:DOPC 2:128. The χ^2 obtained by comparison to experiment indicated that the best Z_{Tat} lay between the simulated values of 16 Å and 18 Å and the best area/lipid A_L lay between the simulated values of 72 $Å^2$ and 74 $Å^2$, so averages were obtained from these four combinations of Z_{Tat} and A_L, weighted inversely with their χ^2. The average positions, Z'_{Phos}, of phosphates situated underneath the Tats were calculated by averaging over the phosphates whose in-plane distance, R, from the center of Tat is smaller than R_{Tat}. The simulation cell extended to 38Å, far enough to ensure that Z_{Phos} for most of the lipids is the same as for DOPC. Assuming a simple linear ramp in Z_{Phos}, **Fig. 9** then indicates a ring of boundary lipids that extends twice are far in R as Tat itself. Although the guanidinium electron density profile was broad (**Fig. S8**), indicating that some were pointing away from the bilayer

relative to the center of Tat, more were pointing towards the bilayer center as indicated in **Fig. 9**. Numerical values are given in **Table S1**.

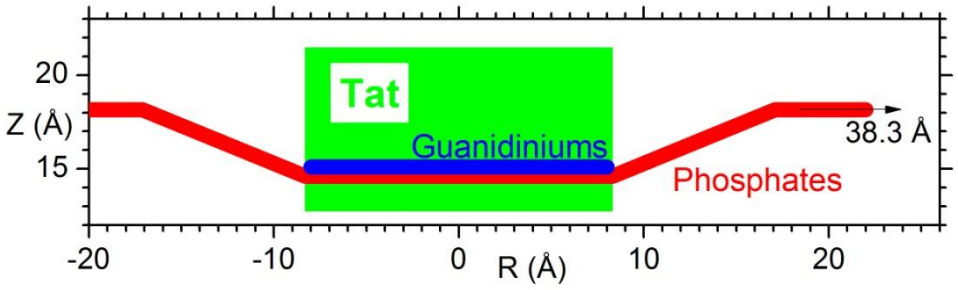

Figure 9. Location of Tat in DOPC bilayer. Tat is represented as a cylinder, Z is the distance from the bilayer center, and R is the in-plane distance from the center of Tat. The average Z of the lipid phosphates as a function of R and the arginine guanidiniums are shown in red and blue, respectively.

4. Discussion

Given that 8 of the 11 amino acids in Tat (47-57) are arginines and lysines, one would have suggested 20 years ago that highly charged Tat would partition strongly into solution rather than being associated with lipid bilayers. By contrast, but in agreement with more recent perspectives on arginine partitioning into the interfacial region [58], we find that Tat interacts with lipid bilayers, even with neutral DOPC and DOPC/DOPE mixtures, as well as with negatively charged DOPC/DOPS and nuclear membrane mimic lipid mixtures. This paper presents multiple lines of evidence for a Tat/membrane interaction. **Fig. 2** shows that Tat decreases the bending modulus. Although one could argue that such a decrease is only apparent and could instead be due to local changes in membrane spontaneous curvature [59], either interpretation supports a Tat-bilayer interaction. The changes with increasing Tat concentration in the X-ray membrane form factors in **Fig. 3** prove that Tat affects membrane structure, and the shift of the zero positions to higher q_z suggests thinning. Thinning is substantiated by quantitative analysis of the X-ray data and by MD simulations. **Fig. 7A** shows that the average membrane thickness, as measured by the distance D_{PP} between phosphocholines on opposite surfaces, decreases with increasing Tat concentration. Similar thinning is shown in **Fig. 7B** for the distance D_{HH} between the maxima in the electron density profiles of opposite surfaces. Compared to D_{PP}, D_{HH} is pulled towards both the carbonyl/glycerol groups and Tat because both have electron densities (~0.4 e/Å^3) greater than water (~0.33 e/Å^3) or hydrocarbon (~0.3 e/Å^3). Although the thinning shown in **Figs. 7A** and **7B** is not large, it obviously requires interaction of Tat with the bilayers. **Fig. 7C** shows that A_L increases with increasing Tat concentration, by both model fitting and MD simulations.

It is of considerable interest to learn where Tat resides, on average, in the membrane, as this would establish a base position from which translocation would be initiated. We have combined our two main methods, MD simulations and X-ray scattering, to address this question.

In general, Tats locate at the bilayer/water interface as indicated in Section *3.2*, and they are close to the phosphocholine headgroup region by comparing the simulated $2Z_{Tat}$ in **Fig. 7.D** with **7.A.** Although the SDP modeling of the X-ray data obtains excellent fits to the experimental form factors for a model with Tat deep in the hydrocarbon interior (see **Fig. S5**), the corresponding MD simulation (shown in **Fig. 4.C**) eliminates this spurious result. **Fig. 7D** also shows that modeling gives smaller values for Z_{Tat} than the simulation. The modeling result is supportive of the original simulation result of Herce and Garcia that Tat resides closer to the bilayer center than do the phosphocholine groups [60]. That is a base position that would be a possibly important precursor to translocation, as would the larger A_L.

Several groups have carried out calculations and MD simulations showing that the cost of moving an arginine group from water to the bilayer center is ~12-26 kcal/mol [58, 61-63] or 6-7 kcal/mol if side-chain snorkeling to the surface is taken into account [64]. This is not inconsistent with our result that Tat interacts with the membrane because, as is well known, the bilayer is not just a hydrocarbon slab, but has interfacial headgroup regions where Tat can reside. It has been suggested that the free energy cost for charged amino acids entering the headgroup region is similar to that for partitioning into octanol, about an order of magnitude smaller free energy cost than partitioning into cyclohexane [65-67]. Simulations suggest that the free energy is smaller for an arginine residing in the interfacial region than in water, roughly by 3 kcal/mole, depending upon the lipid [58, 67]. Our results therefore appear energetically reasonable.

One concern with diffraction experiments on samples consisting of adjacent bilayers in a stack or in a multilamellar vesicle is that the samples have to be partially dried to obtain conventional diffraction data. But then there is no pure water layer between adjacent bilayers, so a hydrophilic peptide is forced into the interfacial, partially hydrophilic region of the lipid bilayer. In contrast, by using diffuse scattering, we obtained structure from experimental samples that had a range of lamellar D spacings (see **Fig. 2** caption) that were considerably larger than the thickness of the bilayer in **Fig. 7A**, thereby providing an ample pure water space, typically greater than 20Å. The result that $2Z_{Tat}$ shown in **Fig. 7D** is so much smaller than our repeat spacings shows that Tat preferentially associates with the membrane rather than dissociating into water.

Consistent with Tat softening the bilayers (**Fig. 2**), it also disorders them as indicated by S_{xray} decreasing with Tat concentration shown in **Fig. 8**. Tat also increases the mosaic spread observed by X-ray and neutron scattering as shown in **Figs. S1-3**; this is a much larger scale disordering of the stack of bilayers. As shown in **Table 1** and in **Fig. S7**, Tat assumed slightly >50% β structures, both when dissolved in water and in contact with a hydrated thin film membrane. Our results were determined using the DichroWEB program, which compares the mean residue ellipticity with that from standard globular proteins, with details given in Supplementary data near **Fig. S7**. These structures include approximately equal amounts of regular β strands and turns, with ~half that amount of distorted β strands. The next most prevalent structure was random coil (~37%). Measurements in the literature (see **Section 1. Introduction**) report a primarily random structure, determined using either CD or NMR. This difference could be due to different sample preparations, or due to a different interpretation of the CD spectra. Ref. [68] reported that CD spectra of unordered polypeptides are similar to that

of the poly(Pro)II helix, and a significant fraction of the unordered conformation in globular proteins consists of poly(Pro)II helix plus distorted β strands.

In an effort to better determine the secondary structure of Tat, our collaborator, Dr. Rieko Ishima, performed 1D and 2D-NMR of Tat in solution at 10, 20 and 30^{o}C. Her results showed no evidence for backbone hydrogen bond formation, indicating that the peptide does not have a stable β conformation, at least on the time scale of the NMR measurement. Additionally, we analyzed the secondary structures of Tats from MD simulations using the Define Secondary Structure of Proteins (DSSP) program [69]. Data from the MD simulation which has the best fit to experimental X-ray form factors show that Tat contains neither β nor α-helix structures. Therefore, both our solution NMR and MD simulation results find primarily random coil, with no significant β structure, which contrasts with our CD findings of >50% β conformation. While the interpretation of CD spectra as β, P2 helix or coil is controversial, what is clear is that the membrane does not influence the conformation of solubilized Tat. In addition, no studies including our own, have implicated Tat forming an α-helix, either in solution or in the membrane.

Given our structural and elastic moduli results, we now compare to other experiments in the literature. In 2008, the Wong group implicated Tat's ability to induce saddle-splay curvature with a potential role of bidentate hydrogen bonding as key [70]. Rhodamine-tagged Tat only entered GUVs when the PE headgroup was included with PS and PC lipids (PS/PC/PE, 20:40:40), indicating that hydrogen-bonding, and/or curvature-promoting lipids are required for Tat translocation. In PS/PE (20:80) lipids, they found Tat caused a highly curved cubic phase using X-ray diffraction [70]. In our experiments, there was little effect of adding DOPE to DOPC at either a 3:1 or 1:1 mole ratio on decrease in the bending modulus, bilayer thinning, Tat's outward movement with increasing concentration or disordering of chains (S_{xray}). Our two results are not inconsistent, however, since curvature-promotion appears not to be required for Tat's ability to lower the energy required to bend, nor to locate Tat in the bilayer, nor to disorder chains, all of which may be important for Tat translocation. Yet Tat does translocate across membranes in their experiments only with PE in the membrane, so the ability to induce saddle-splay curvature may also be required for Tat's translocation. Another study by Melikov et al. [26] found that Tat's main mechanism of action is to induce lipid mixing and membrane leakage with lipids of late endosomes. This result is consistent with our results that Tat induced a reversible, hydration-induced increase in mosaic spread (**Figs. S1-3)** and a disordering of chains **(Fig. 8)**. Both of these could induce lipid mixing and perhaps, membrane leakage. An X-ray, neutron and AFM study reported thickening upon initial Tat binding, in contradiction to our result in **Fig. 7B** that shows thinning [71]. We suggest that this difference was caused by their using stiff gel phase DPPC lipid that did not allow bound Tat to perturb the bilayer. Using a variety of techniques, including high sensitivity isothermal titration calorimetry and ^{2}H- and ^{31}P-NMR, Seelig et al. [72] presented evidence that the lipid bilayer remains intact upon Tat binding and our results confirm this. Finally, we compare our structural results to those obtained by solid state NMR, although at a lower hydration level than in our sample. Hong et al. [32] found that Tat lies parallel to the bilayer surface in the headgroup region of DMPC/DMPG (8:7) bilayers, similar to our cartoon in **Fig. 9**.

Although a recent MD simulation using umbrella sampling [73] found that the free energy required for cR9 to traverse a membrane was smaller if a water pore was present, we cannot directly test the existence of a transient water pore from our X-ray or neutron scattering experiments. This is because, even with a water pore, the translocation process still requires crossing a free energy barrier which is a non-equilibrium process. X-ray form factors measure an equilibrium state. If the form factors obtained from water pore structures agreed well with experiments, it would indicate that the pore structure was thermodynamically stable. This may be the case for some antimicrobial peptides, but certainly not for cell-penetrating peptides.

Finding a kinetically competent pathway for the interesting phenomenon of translocation of highly charged Tat through hydrophobic membranes is difficult. An energetically passive translocation likely occurs very seldom on an MD simulation time scale, and it probably happens quickly, so it would not significantly change the average structure of the membrane in which it occurs. Although our results in this paper do not reveal a kinetically competent pathway, they do show that Tat is drawn to the surface of the membrane, and is therefore ready for translocation at a region of local thinning. And they show that these interactions tend to soften (**Fig. 2**) and disorder (**Fig. 8**) the membrane and increase the A_L, thereby likely reducing the energy barrier for passive translocation.

5. Acknowledgments: Research reported in this publication was supported by the National Institute of General Medical Sciences of the National Institutes of Health under award GM44976 (PIs JFN, STN). and GM86801 (PI AG). The content is solely the responsibility of the authors and does not necessarily represent the official views of the National Institutes of Health. We acknowledge the Cornell High Energy Synchrotron Source (CHESS) which is supported by the National Science Foundation and the NIH/NIGMS under NSF award DMR-0936384. We acknowledge the Center for Molecular Analysis at Carnegie Mellon University for use of the Jasco 715 and for mass spectrometry analysis and the Protein Synthesis Core of the University of Pittsburgh for peptide production. The authors also acknowledge Dr. Rieko Ishima for carrying out NMR measurements, Leah Langer for help using Matlab with the neutron scattering data and Laura Carroll for carrying out CD measurements. We would also like to acknowledge Dr. Jeffery Krzywon at NIST for technical help with our hydration chamber.

References

[1] R. Fischer, M. Fotin-Mleczek, H. Hufnagel, R. Brock, Break on through to the other side-biophysics and cell biology shed light on cell-penetrating peptides, Chembiochem, 6 (2005) 2126-2142. DOI 10.1002/cbic.200500044.
[2] A. Joliot, A. Prochiantz, Transduction peptides: from technology to physiology, Nat Cell Biol, 6 (2004) 189-196. Doi 10.1038/Ncb0304-189.
[3] M. Lindgren, M. Hallbrink, A. Prochiantz, U. Langel, Cell-penetrating peptides, Trends Pharmacol Sci, 21 (2000) 99-103. DOI S0165-6147(00)01447-4.
[4] A.D. Frankel, C.O. Pabo, Cellular uptake of the tat protein from human immunodeficiency virus, Cell, 55 (1988) 1189-1193. DOI 0092-8674(88)90263-2.
[5] M. Green, P.M. Loewenstein, Autonomous functional domains of chemically synthesized human immunodeficiency virus tat trans-activator protein, Cell, 55 (1988) 1179-1188. DOI 0092-8674(88)90262-0.
[6] E. Vives, P. Brodin, B. Lebleu, A truncated HIV-1 Tat protein basic domain rapidly translocates through the plasma membrane and accumulates in the cell nucleus, J Biol Chem, 272 (1997) 16010-16017. DOI: 10.1074/jbc.272.25.16010.
[7] G. Ter-Avetisyan, G. Tunnemann, D. Nowak, M. Nitschke, A. Herrmann, M. Drab, M.C. Cardoso, Cell entry of arginine-rich peptides is independent of endocytosis, J Biol Chem, 284 (2009) 3370-3378. Doi 10.1074/jbc.M805550200.
[8] F. Duchardt, M. Fotin-Mleczek, H. Schwarz, R. Fischer, R. Brock, A comprehensive model for the cellular uptake of cationic cell-penetrating peptides, Traffic, 8 (2007) 848-866. DOI: 10.1111/j.1600-0854.2007.00572.x.
[9] G. Tunnemann, R.M. Martin, S. Haupt, C. Patsch, F. Edenhofer, M.C. Cardoso, Cargo-dependent mode of uptake and bioavailability of TAT-containing proteins and peptides in living cells, Faseb J, 20 (2006) 1775-1784. DOI: 10.1096/fj.05-5523com.
[10] A. Ziegler, P. Nervi, M. Durrenberger, J. Seelig, The cationic cell-penetrating peptide Cpp(TAT) derived from the HIV-1 protein TAT is rapidly transported into living fibroblasts: Optical, biophysical, and metabolic evidence, Biochemistry, 44 (2005) 138-148. Doi 10.1021/Bi0491604.
[11] J.S. Wadia, R.V. Stan, S.F. Dowdy, Transducible TAT-HA fusogenic peptide enhances escape of TAT-fusion proteins after lipid raft macropinocytosis, Nat Med, 10 (2004) 310-315. DOI 10.1038/nm996nm996.

[12] I.M. Kaplan, J.S. Wadia, S.F. Dowdy, Cationic TAT peptide transduction domain enters cells by macropinocytosis, J Control Release, 102 (2005) 247-253. DOI S0168-3659(04)00476-6 [pii]10.1016/j.jconrel.2004.10.018.

[13] D.A. Mann, A.D. Frankel, Endocytosis and targeting of exogenous HIV-1 Tat protein, Embo J, 10 (1991) 1733-1739.
[14] J.P. Richard, K. Melikov, H. Brooks, P. Prevot, B. Lebleu, L.V. Chernomordik, Cellular uptake of unconjugated TAT peptide involves clathrin-dependent endocytosis and heparan sulfate receptors, J Biol Chem, 280 (2005) 15300-15306. DOI 10.1074/jbc.M401604200.

[15] S.W. Jones, R. Christison, K. Bundell, C.J. Voyce, S.M. Brockbank, P. Newham, M.A. Lindsay, Characterisation of cell-penetrating peptide-mediated peptide delivery, Br J Pharmacol, 145 (2005) 1093-1102. DOI 10.1038/sj.bjp.0706279.

[16] A. Vendeville, F. Rayne, A. Bonhoure, N. Bettache, P. Montcourrier, B. Beaumelle, HIV-1 Tat enters T cells using coated pits before translocating from acidified endosomes and eliciting biological responses, Mol Biol Cell, 15 (2004) 2347-2360. DOI 10.1091/mbc.E03-12-0921.

[17] C. Foerg, U. Ziegler, J. Fernandez-Carneado, E. Giralt, R. Rennert, A.G. Beck-Sickinger, H.P. Merkle, Decoding the entry of two novel cell-penetrating peptides in HeLa cells: lipid raft-mediated endocytosis and endosomal escape, Biochemistry-Us, 44 (2005) 72-81. DOI 10.1021/bi048330+.
[18] A. Fittipaldi, M. Giacca, Transcellular protein transduction using the Tat protein of HIV-1, Adv Drug Deliv Rev, 57 (2005) 597-608. S DOI 0169-409X(04)00269-8

[19] Y. Liu, M. Jones, C.M. Hingtgen, G.J. Bu, N. Laribee, R.E. Tanzi, R.D. Moir, A. Nath, J.J. He, Uptake of HIV-1 Tat protein mediated by low-density lipoprotein receptor-related protein disrupts the neuronal metabolic balance of the receptor ligands, Nature Medicine, 6 (2000) 1380-1387.
[20] V.P. Torchilin, R. Rammohan, V. Weissig, T.S. Levchenko, TAT peptide on the surface of liposomes affords their efficient intracellular delivery even at low temperature and in the presence of metabolic inhibitors, Proc Natl Acad Sci U S A, 98 (2001) 8786-8791. DOI 10.1073/pnas.151247498.

[21] V.P. Torchilin, T.S. Levchenko, R. Rammohan, N. Volodina, B. Papahadjopoulos-Sternberg, G.G. D'Souza, Cell transfection in vitro and in vivo with nontoxic TAT peptide-liposome-DNA complexes, Proc Natl Acad Sci U S A, 100 (2003) 1972-1977. DOI 10.1073/pnas.0435906100.

[22] C. Rudolph, C. Plank, J. Lausier, U. Schillinger, R.H. Muller, J. Rosenecker, Oligomers of the arginine-rich motif of the HIV-1 TAT protein are capable of transferring plasmid DNA into cells, J Biol Chem, 278 (2003) 11411-11418. DOI 10.1074/jbc.M211891200.

[23] A. Chauhan, A. Tikoo, A.K. Kapur, M. Singh, The taming of the cell penetrating domain of the HIV Tat: myths and realities, J Control Release, 117 (2007) 148-162. DOI 10.1016/j.jconrel.2006.10.031.

[24] J.M. Sabatier, E. Vives, K. Mabrouk, A. Benjouad, H. Rochat, A. Duval, B. Hue, E. Bahraoui, Evidence for neurotoxic activity of tat from human immunodeficiency virus type 1, J Virol, 65 (1991) 961-967.
[25] A. Mishra, V.D. Gordon, L. Yang, R. Coridan, G.C. Wong, HIV TAT forms pores in membranes by inducing saddle-splay curvature: potential role of bidentate hydrogen bonding, Angew Chem Int Ed Engl, 47 (2008) 2986-2989. DOI 10.1002/anie.200704444.
[26] S.T. Yang, E. Zaitseva, L.V. Chernomordik, K. Melikov, Cell-penetrating peptide induces leaky fusion of liposomes containing late endosome-specific anionic lipid, Biophysical Journal, 99 (2010) 2525-2533. DOI 10.1016/j.bpj.2010.08.029.
[27] P.E.G. Thoren, D. Persson, E.K. Esbjorner, M. Goksor, P. Lincoln, B. Norden, Membrane binding and translocation of cell-penetrating peptides, Biochemistry, 43 (2004) 3471-3489. Doi 10.1021/Bi0360049.
[28] S.D. Kramer, H. Wunderli-Allenspach, No entry for TAT(44-57) into liposomes and intact MDCK cells: novel approach to study membrane permeation of cell-penetrating peptides, Biochimica Et Biophysica Acta-Biomembranes, 1609 (2003) 161-169. Doi 10.1016/S0005-2736(02)00683-1.
[29] C. Ciobanasu, J.P. Siebrasse, U. Kubitscheck, Cell-penetrating HIV1 TAT peptides can generate pores in model membranes, Biophysical Journal, 99 (2010) 153-162. DOI 10.1016/j.bpj.2010.03.065.

[30] P.A. Gurnev, S.T. Yang, K.C. Melikov, L.V. Chernomordik, S.M. Bezrukov, Cationic cell-penetrating peptide binds to planar lipid bilayers containing negatively charged lipids but does not induce conductive pores, Biophys J, 104 (2013) 1933-1939. DOI 10.1016/j.bpj.2013.02.053.

[31] H.D. Herce, A.E. Garcia, J. Litt, R.S. Kane, P. Martin, N. Enrique, A. Rebolledo, V. Milesi, Arginine-Rich Peptides Destabilize the Plasma Membrane, Consistent with a Pore Formation Translocation Mechanism of Cell-Penetrating Peptides, Biophysical Journal, 97 (2009) 1917-1925. DOI 10.1016/j.bpj.2009.05.066.
[32] Y.C. Su, A.J. Waring, P. Ruchala, M. Hong, Membrane-bound dynamic structure of an arginine-rich cell-penetrating peptide, the protein transduction domain of HIV Tat, from solid-state NMR, Biochemistry, 49 (2010) 6009-6020. Doi 10.1021/Bi100642n.
[33] S. Shojania, J.D. O'Neil, HIV-1 Tat is a natively unfolded protein - The solution conformation and dynamics of reduced HIV-1 Tat-(1-72) by NMR spectroscopy, J Biol Chem, 281 (2006) 8347-8356. DOI 10.1074/jbc.M510748200.
[34] P. Bayer, M. Kraft, A. Ejchart, M. Westendorp, R. Frank, P. Rosch, Structural studies of Hiv-1 tat protein, J Mol Biol, 247 (1995) 529-535. Doi 10.1016/S0022-2836(05)80133-0.
[35] H.D. Herce, A.E. Garcia, Molecular dynamics simulations suggest a mechanism for translocation of the HIV-1 TAT peptide across lipid membranes, Proc Natl Acad Sci U S A, 104 (2007) 20805-20810. DOI10.1073/pnas.0706574105.

[36] S. Yesylevskyy, S.J. Marrink, A.E. Mark, Alternative mechanisms for the interaction of the cell-penetrating peptides penetratin and the TAT peptide with lipid bilayers, Biophysical Journal, 97 (2009) 40-49. DOI 10.1016/j.bpj.2009.03.059.
[37] E.D. Jarasch, C.E. Reilly, P. Comes, J. Kartenbeck, W.W. Franke, Isolation and characterization of nuclear membranes from calf and rat thymus, Hoppe Seylers Z Physiol Chem, 354 (1973) 974-986.
[38] S.A. Tristram-Nagle, Preparation of oriented, fully hydrated lipid samples for structure determination using X-ray scattering, Methods Mol Biol, 400 (2007) 63-75.
[39] N. Kučerka, Y.F. Liu, N.J. Chu, H.I. Petrache, S. Tristram-Nagle, J.F. Nagle, Structure of fully hydrated fluid phase DMPC and DLPC lipid bilayers using X-ray scattering from oriented multilamellar arrays and from unilamellar vesicles, Biophysical Journal, 88 (2005) 2626-2637.
[40] K. He, S.J. Ludtke, W.T. Heller, H.W. Huang, Mechanism of alamethicin insertion into lipid bilayers, Biophysical Journal, 71 (1996) 2669-2679.
[41] S. Schick, L.R. Chen, E. Li, J. Lin, I. Koper, K. Hristova, Assembly of the M2 tetramer Is strongly modulated by lipid chain length, Biophysical Journal, 99 (2010) 1810-1817. DOI 10.1016/j.bpj.2010.07.026.
[42] Y.F. Liu, J.F. Nagle, Diffuse scattering provides material parameters and electron density profiles of biomembranes, Phys Rev E, 69 (2004) 040901-040904(R). DOI 10.1103/Physreve.69.040901.
[43] Y. Lyatskaya, Y.F. Liu, S. Tristram-Nagle, J. Katsaras, J.F. Nagle, Method for obtaining structure and interactions from oriented lipid bilayers, Phys Rev E, 63 (2001) 0119071-0119079.
[44] N. Kučerka, J.F. Nagle, J.N. Sachs, S.E. Feller, J. Pencer, A. Jackson, J. Katsaras, Lipid bilayer structure determined by the simultaneous analysis of neutron and x-ray scattering data, Biophys J, 95 (2008) 2356-2367. DOI 10.1529/biophysj.108.132662.
[45] T.T. Mills, G.E.S. Toombes, S. Tristram-Nagle, D.M. Smilgies, G.W. Feigenson, J.F. Nagle, Order parameters and areas in fluid-phase oriented lipid membranes using wide angle x-ray scattering, Biophysical Journal, 95 (2008) 669-681. DOI 10.1529/biophysj.107.127845.
[46] T.T. Mills, S. Tristram-Nagle, F.A. Heberle, N.F. Morales, J. Zhao, J. Wu, G.E.S. Toombes, J.F. Nagle, G.W. Feigenson, Liquid-liquid domains in bilayers detected by wide angle x-ray scattering, Biophysical Journal, 95 (2008) 682-690. DOI 10.1529/biophysj.107.127910.
[47] M. Raghunathan, Y. Zubovski, R.M. Venable, R.W. Pastor, J.F. Nagle, S. Tristram-Nagle, Structure and Elasticity of Lipid Membranes with Genistein and Daidzein Bioflavinoids Using X-ray Scattering and MD Simulations, Journal of Physical Chemistry B, 116 (2012) 3918-3927. Doi 10.1021/Jp211904j.

[48] A.L. Boscia, K. Akabori, Z. Benamram, J.A. Michel, M.S. Jablin, J.D. Steckbeck, R.C. Montelaro, J.F. Nagle, S. Tristram-Nagle, Membrane structure correlates to function of LLP2 on the cytoplasmic tail of HIV-1 gp41 protein, Biophysical Journal, 105 (2013) 657-666. DOI 10.1016/j.bpj.2013.06.042.
[49] B. Hess, C. Kutzner, D. van der Spoel, E. Lindahl, GROMACS 4: Algorithms for highly efficient, load-balanced, and scalable molecular simulation, J Chem Theory Comput, 4 (2008) 435-447. Doi 10.1021/Ct700301q.
[50] J.P. Jambeck, A.P. Lyubartsev, Derivation and systematic validation of a refined all-atom force field for phosphatidylcholine lipids, The journal of physical chemistry. B, 116 (2012) 3164-3179. DOI 10.1021/jp212503e.
[51] J.P.M. Jambeck, A.P. Lyubartsev, An extension and further validation of an all-atomistic force field for biological membranes, J Chem Theory Comput, 8 (2012) 2938-2948. Doi 10.1021/Ct300342n.
[52] V. Hornak, R. Abel, A. Okur, B. Strockbine, A. Roitberg, C. Simmerling, Comparison of multiple amber force fields and development of improved protein backbone parameters, Proteins, 65 (2006) 712-725. Doi 10.1002/Prot.21123.
[53] W.L. Jorgensen, J. Chandrasekhar, J.D. Madura, R.W. Impey, M.L. Klein, Comparison of simple potential functions for simulating liquid water, J Chem Phys, 79 (1983) 926-935. Doi 10.1063/1.445869.
[54] N. Kučerka, J. Katsaras, J.F. Nagle, Comparing membrane simulations to scattering experiments: introducing the SIMtoEXP software, J Membr Biol, 235 (2010) 43-50. DOI 10.1007/s00232-010-9254-5.
[55] N. Kučerka, S. Tristram-Nagle, J.F. Nagle, Closer look at structure of fully hydrated fluid phase DPPC bilayers, Biophysical Journal, 90 (2006) L83-L85. DOI 10.1529/biophysj.106.086017.
[56] N. Kučerka, S. Tristram-Nagle, J.F. Nagle, Structure of fully hydrated fluid phase lipid bilayers with monounsaturated chains, J Membrane Biol, 208 (2005) 193-202. DOI 10.1007/s00232-005-7006-8.
[57] S. Tristram-Nagle, C.P. Yang, J.F. Nagle, Thermodynamic studies of purple membrane, Biochim Biophys Acta, 854 (1986) 58-66. Doi 10.1016/0005-2736(86)90064-7.
[58] A.C.V. Johansson, E. Lindahl, The role of lipid composition for insertion and stabilization of amino acids in membranes, J Chem Phys, 130 (2009) Doi 10.1063/1.3129863.

[59] S. Tristram-Nagle, J.F. Nagle, HIV-1 fusion peptide decreases bending energy and promotes curved fusion intermediates, Biophysical Journal, 93 (2007) 2048-2055. DOI 10.1529/biophysj.107.109181.
[60] H.D. Herce, A.E. Garcia, Molecular dynamics simulations suggest a mechanism for translocation of the HIV-1 TAT peptide across lipid membranes, P Natl Acad Sci USA, 104 (2007) 20805-20810. DOI 10.1073/pnas.0706574105.
[61] L.B. Li, I. Vorobyov, T.W. Allen, Potential of mean force and pK(a) profile calculation for a lipid membrane-exposed arginine side chain, Journal of Physical Chemistry B, 112 (2008) 9574-9587. Doi 10.1021/Jp7114912.
[62] I. Vorobyov, L.B. Li, T.W. Allen, Assessing atomistic and coarse-grained force fields for protein-lipid interactions: The formidable challenge of an ionizable side chain in a membrane, Journal of Physical Chemistry B, 112 (2008) 9588-9602. Doi 10.1021/Jp711492h.
[63] J.L. MacCallum, W.F.D. Bennett, D.P. Tieleman, Distribution of amino acids in a lipid bilayer from computer simulations, Biophysical Journal, 94 (2008) 3393-3404. DOI 10.1529/biophysj.107.112805.
[64] E.V. Schow, J.A. Freites, P. Cheng, A. Bernsel, G. von Heijne, S.H. White, D.J. Tobias, Arginine in membranes: The connection between molecular dynamics simulations and translocon-mediated insertion experiments, J Membrane Biol, 239 (2011) 35-48. DOI 10.1007/s00232-010-9330-x.
[65] W.C. Wimley, T.P. Creamer, S.H. White, Solvation energies of amino acid side chains and backbone in a family of host-guest pentapeptides, Biochemistry, 35 (1996) 5109-5124. Doi 10.1021/Bi9600153.
[66] W.C. Wimley, S.H. White, Experimentally determined hydrophobicity scale for proteins at membrane interfaces, Nat Struct Biol, 3 (1996) 842-848.

[67] B. Roux, Lonely arginine seeks friendly environment, J Gen Physiol, 130 (2007) 233-236. DOI 10.1085/jgp.200709819.
[68] N. Sreerama, R.W. Woody, Structural composition of beta(I)- and beta(II)-proteins, Protein Sci, 12 (2003) 384-388. Doi 10.1110/Ps.0235003.
[69] W. Kabsch, C. Sander, Dictionary of protein secondary structure: pattern recognition of hydrogen-bonded and geometrical features, Biopolymers, 22 (1983) 2577-2637. DOI 10.1002/bip.360221211.
[70] A. Mishra, V.D. Gordon, L.H. Yang, R. Coridan, G.C.L. Wong, HIV TAT forms pores in membranes by inducing saddle-splay curvature: Potential role of bidentate hydrogen bonding, Angew Chem Int Edit, 47 (2008) 2986-2989. DOI 10.1002/anie.200704444.
[71] D. Choi, J.H. Moon, H. Kim, B.J. Sung, M.W. Kim, G.Y. Tae, S.K. Satija, B. Akgun, C.J. Yu, H.W. Lee, D.R. Lee, J.M. Henderson, J.W. Kwong, K.L. Lam, K.Y.C. Lee, K. Shin, Insertion mechanism of cell-penetrating peptides into supported phospholipid membranes revealed by X-ray and neutron reflection, Soft Matter, 8 (2012) 8294-8297. Doi 10.1039/C2sm25913c.
[72] A. Ziegler, X.L. Blatter, A. Seelig, J. Seelig, Protein transduction domains of HIV-1 and SIV TAT interact with charged lipid vesicles. Binding mechanism and thermodynamic analysis, Biochemistry, 42 (2003) 9185-9194.
[73] K. Huang, A.E. Garcia, Free Energy of Translocating an Arginine-Rich Cell-Penetrating Peptide across a Lipid Bilayer Suggests Pore Formation, Biophysical Journal, 104 (2013) 412-420. DOI 10.1016/j.bpj.2012.10.027.

Supplementary data for HIV-1 Tat membrane interaction probed using X-ray and neutron scattering, CD, and MD simulations

Kiyotaka Akabori[1], Kun Huang[2], Bradley W. Treece[1], Michael S. Jablin[1], Brian Maranville[3], Arthur Woll[4], John F. Nagle[1], Angel E. Garcia[2], and Stephanie Tristram-Nagle[1]

[1]Department of Physics, Carnegie Mellon University, 5000 Forbes Avenue, Pittsburgh, Pennsylvania, [2]Department of Physics, Rensselaer Polytechnic Institute, 110 Eighth Street, Troy, NY 12180, [3]NIST Center for Neutron Research, 100 Bureau Drive, Stop 6102, Gaithersburg, MD 20899, [4]CHESS, Cornell University, 161 Synchrotron Drive, Ithaca, NY 14853

1. Mosaic spread caused by Tat

As hydration proceeded, the mosaic spread, or degree of misorientation, increased. This was apparent by the increasing lengths of the arcs emanating out from the h=1 and h=2 lamellar orders, shown in **Fig. S1**. Mosaic spread was determined by examining lamellar orders in the LAXS CCD position. Matlab was used to plot the intensity of a lamellar order as a function of η, the angle off the meridian. The intensity data above and below the lamellar order were averaged and subtracted from the intensity at the lamellar order to remove diffuse scattering. The subtracted data were fit with a Voigtian function, setting the Gaussian width to the beam width, and extracting the Lorentzian width (ω_L). Then, the following equation was applied to obtain α, $\omega_L^2 = \alpha^2 + 4(\gamma - \theta_B)^2$, where γ=angle of incidence and θ_B is half the scattering angle of the lamellar order. These results are included in Fig. S2, as a function of time after stopping the helium flow and beginning the hydration. The cooling Peltier was at first set to 200 mAmps, which caused the lamellar D-spacing to increase. It was then decreased to 100 mAmps, which caused less water to condense into the sample, and the lamellar D-spacing decreased, as did the mosaic spread. Thus, Tat's ability to disrupt the bilayers appears to be a reversible effect, dependent on the hydration of the sample.

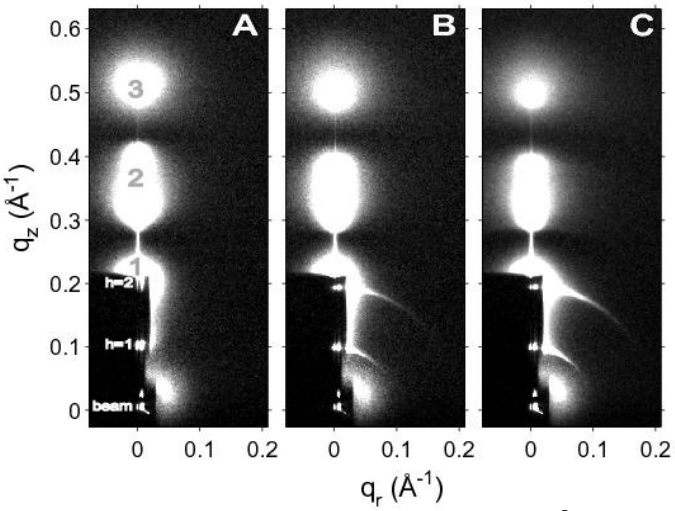

Figure S1. Hydration of DOPC/DOPE (1:1), x=0.034 Tat, 37°C. **A.** Lamellar D-spacing = 60.6 Å, **B.** 65.4 Å, **C.** 65.3 Å. Mosaic spread increases with hydration, shown by visible lengthening of thin arcs near h=1 and h=2 in **B** and **C**. White lobes of diffuse scattering intensity have large grey numbers, while lamellar orders and beam are shown to the left of the Molybdenum beam attenuator (short, dark rectangle).

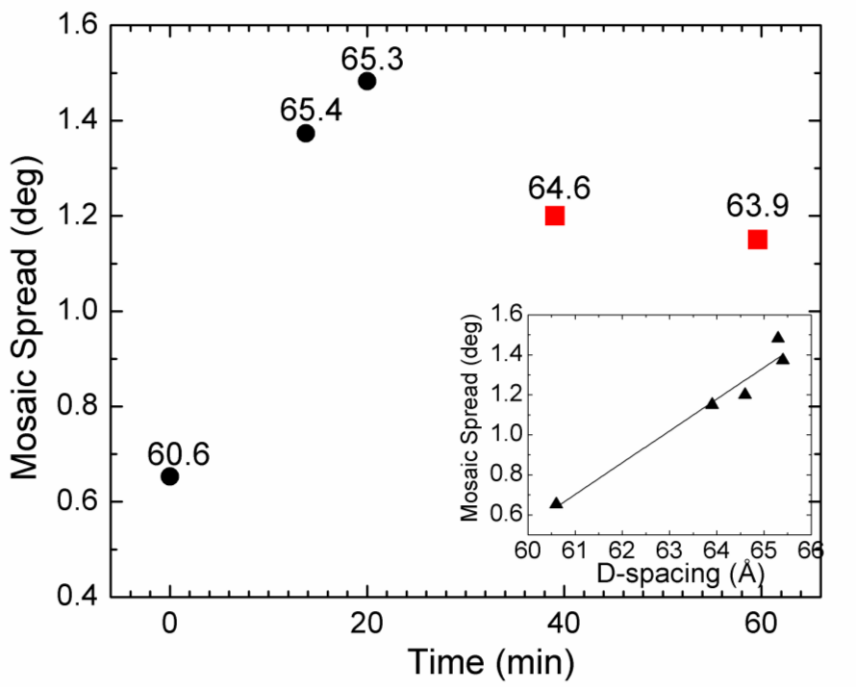

Figure S2. Mosaic spread as a function of time of hydration of DOPC/DOPE (1:1) x=0.034 Tat. Cooling Peltier setting was changed from 200 mAmps (black circles) to 100 mAmps (red squares). Numbers are the lamellar D-spacing (Å). Inset shows that mosaic spread and D-spacing are linearly related.

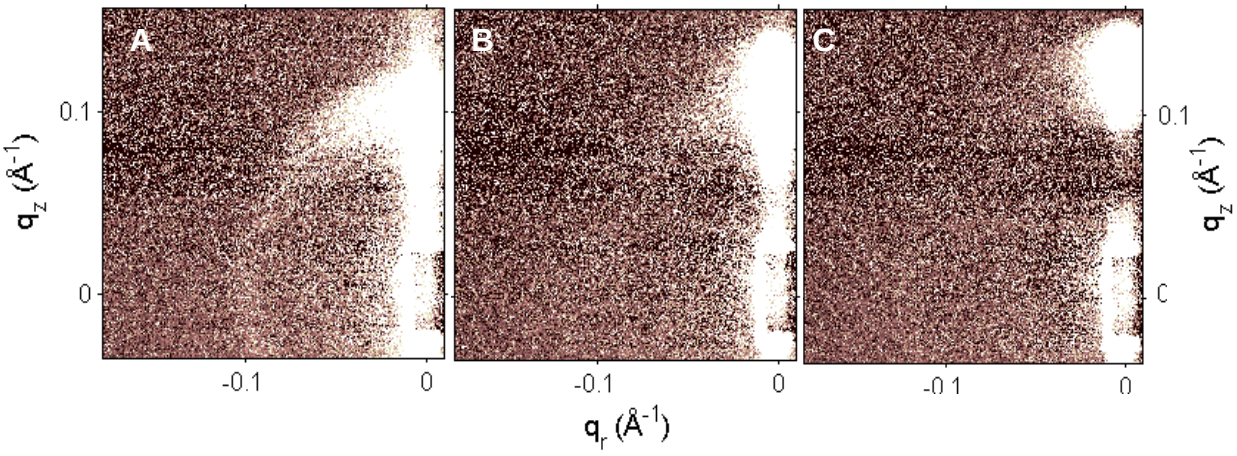

Figure S3. Neutron scattering from stacks of DOPC:DOPE (3:1)/Tat, x=0.059 on a Si substrate hydrated from D_2O vapor. Angle of incidence was 2.4^o and temperature was 37^{o}C. D-spacings were **A.** 63.7 Å, **B.** 57.6, **C.** 49.1 Å. The disappearance of the extensive arc emanating from the first lamellar order as the sample dries, indicates that the misorientation of layers in a stack is a reversible process with hydration, similar to that observed using X-rays.

2. WAXS analysis and results

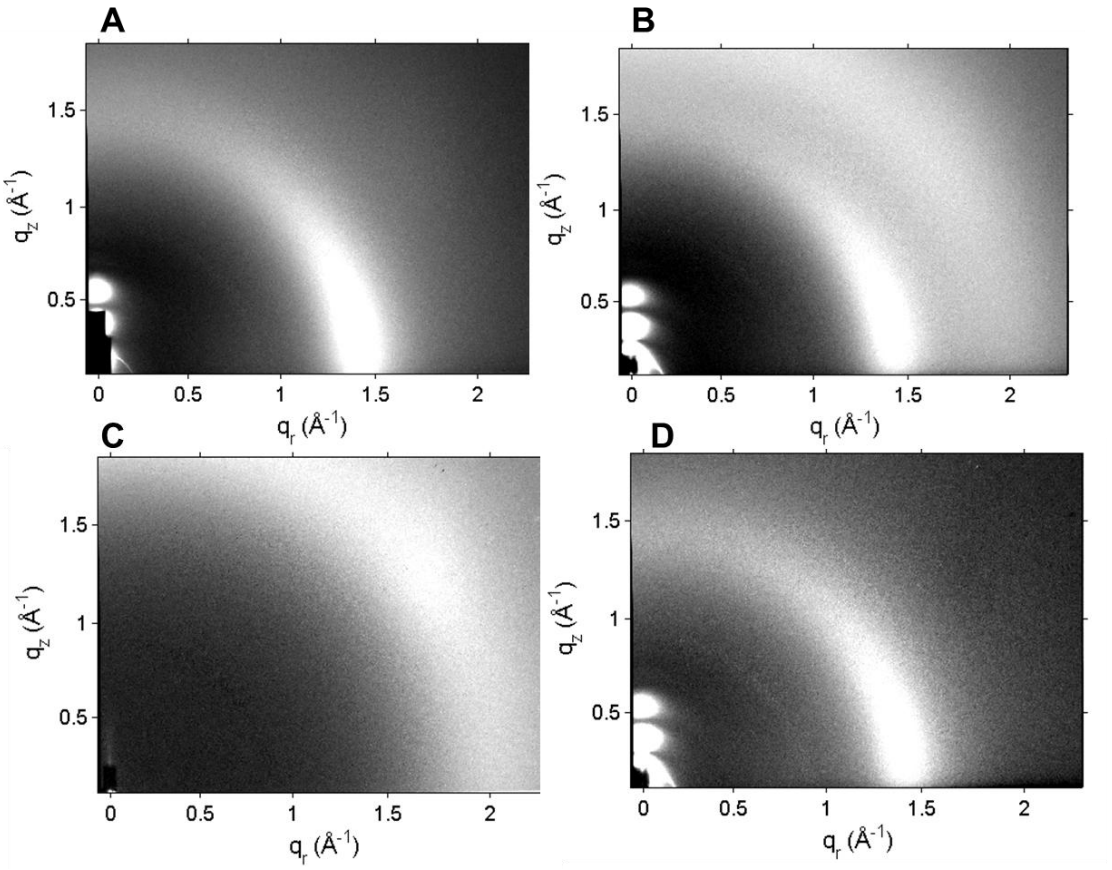

Figure S4. Effect of hydration on WAXS data. **A.** WAXS of a fairly dry sample, lamellar D-spacing = 59.7 Å. **B.** After 15 minutes hydrating with a cooling Peltier setting of 300 mAmps, D = 66.1 Å. **C.** WAXS of water condensed from the vapor onto a silicon wafer. **D.** Sample in **B.** with water removed by subtracting a fraction of condensed water from **C.**

Before the WAXS analysis was carried out, water scattering (shown in **Fig. S4.B,C**) was necessarily removed. Water condenses from the vapor during sample hydration due to the well-insulated hydration chamber and a Peltier cooler located under the sample. As the lamellar D-spacing swells, condensed water appears as a broad, isotropic, diffuse band centered at **q**=2 Å^{-1}. This band is close to the chain correlation WAXS, which is used to obtain the order parameter, S_{xray}, so it is necessary to remove the water scattering prior to analyzing chain WAXS. This is done by quantitatively matching the water scattering in **Fig. S4.B** with a fraction of that in **Fig. S4.C**, and subtracting the water out. We found that hydrated samples are less ordered than drier samples, which suggests that a hydrated sample with the water subtracted out, as in **Fig. S4.D**, is the appropriate one to use for our analysis.

Briefly, WAXS allows calculation of the orientational order parameter, S_{xray}, similar to an NMR order parameter. Mosaic spread α decreases the apparent value of $S_{xray,}$ since misoriented layers will contribute to the diffuse arc emanating up from the equator (see **Fig. S4.B**) (manuscript in preparation). Mosaic spread was determined by examining lamellar orders in the

LAXS CCD position as described in **Section S1**. Matlab was used to plot the intensity of a lamellar order as a function of η, the angle off the meridian. The intensity data above and below the lamellar order were averaged and subtracted from the intensity at the lamellar order to remove diffuse scattering. The subtracted data were fit with a Voigtian function, setting the Gaussian width to the beam width, and extracting the Lorentzian width (ω_L). Then, the following equation was applied to obtain α: $\omega_L^2 = \alpha^2 + 4(\gamma - \theta_B)^2$, where γ=angle of incidence and θ_B=half the scattering angle of the lamellar order.

We used α to correct the decrease of S_{xray} due to mosaic spread, by first plotting S_{xray} values vs. mosaic spread. This was done purely from a theoretical model of how mosaic spread redistributes intensity in the phi direction (manuscript in preparation). We then used these results to interpolate to the value of S_{xray} without mosaic spread given the apparent value of S_{xray} and α for the sample. In order to track the behavior of apparent S_{xray} values over a larger range, mock S_{xray} data were created with different values of S_{xray}, and a Lorentzian weight distribution of smearing the intensity measured from the CCD image was applied to the mock data. S_{xray} was then determined again on the smeared mock data and this new value was assigned to the original S_{xray} value and α. By obtaining smeared S_{xray} values over a wide range of mock data and mosaic spreads, many measured values of S_{xray} and α from the experimental data could be corrected to values of S_{xray} without mosaic spread. The corrections to S_{xray} due to mosaic spread were ~5-8%.

3. Alternative location of Tat from SDP modeling alone

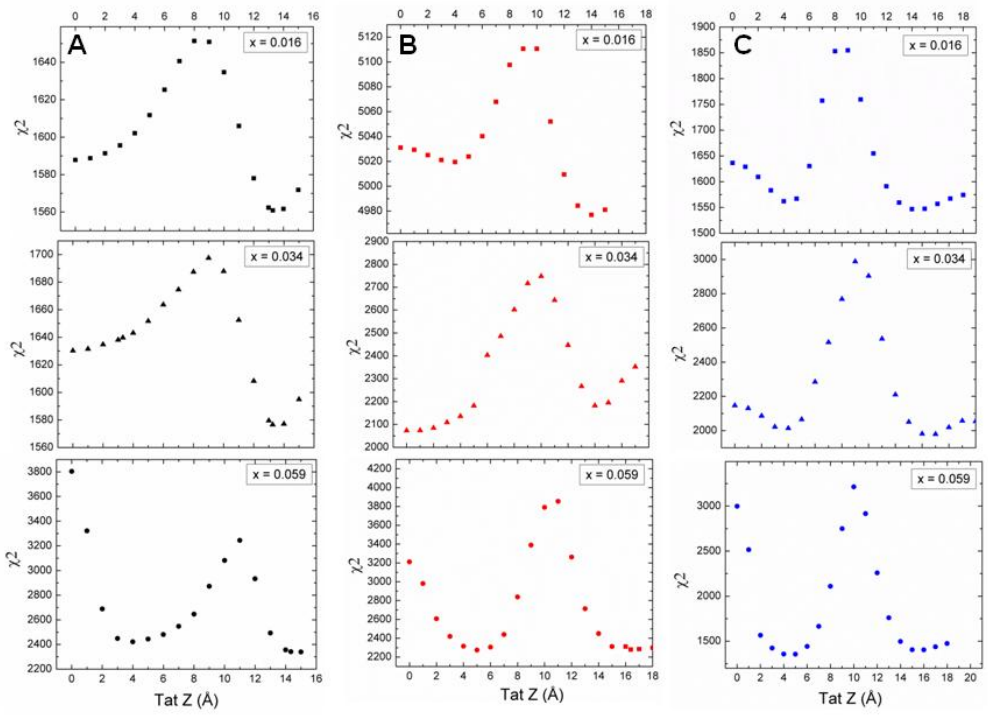

Figure S5. Chi-square as a function of Tat position Z across the bilayer. **A**. DOPC, **B**. DOPC:DOPE (3:1), **C**. DOPC:DOPE (1:1).

In addition to allowing the Tat position to move freely during the SDP fit to the form factor data, we can also fix Tat's position. In order to determine the location of Tat in these membrane mimics, the Tat position Z is fixed in 1 Å steps and the resulting chi-square from the SDP model fit is plotted as shown in **Fig. S5**. As shown, more than one minimum occurred for some of the lipid mixtures and Tat concentrations. In addition to the headgroup location for Tat, there was a second best fit locating Tat in the interior of the hydrocarbon at ~4-5 Å from the bilayer center. This position had an equally good chi-square as the headgroup position in DOPC:DOPE (3:1) and DOPC:DOPE (1:1) at x = 0.059. In general, the Tat interior position was favored at higher Tat concentrations and in mimics with DOPE. For DOPC mixtures, the Tat hydrocarbon position did not fit the data as well as the headgroup position, even at x = 0.059. Thinning of the bilayers was identical with Tat in the hydrocarbon position. Electron density profiles with Tat in the hydrocarbon interior are shown in **Fig. S6**.

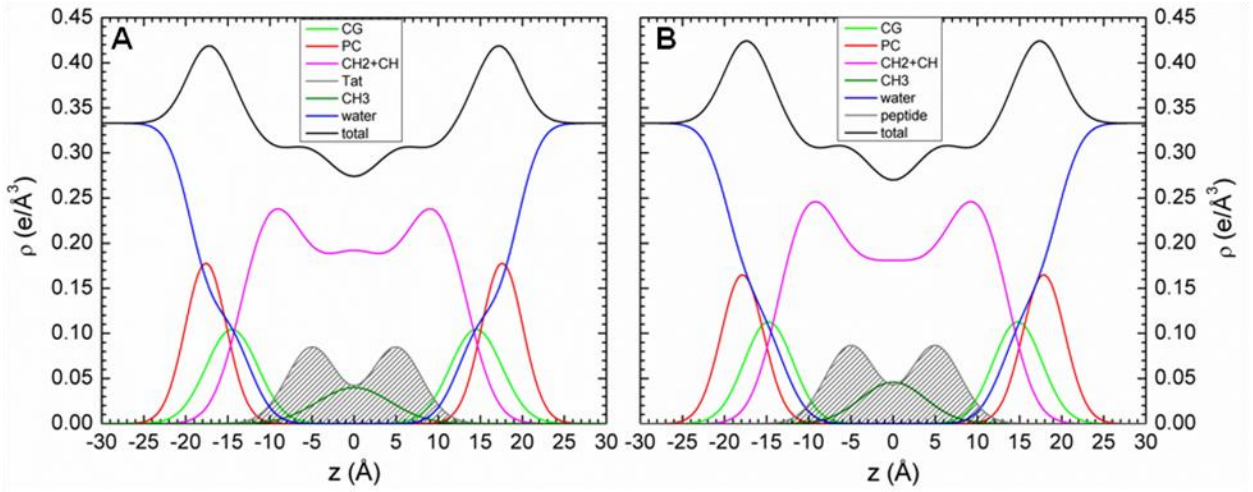

Figure S6. Electron density profiles with Tat in the hydrocarbon interior. **A.** DOPC/DOPE(3:1), x= 0.059 **B.** DOPC/DOPE(1:1), x= 0.059.

Although our SDP model fitting does find these equally low chi-square values when fixing Tat at discrete positions across the bilayer, a free fit does not locate Tat in the hydrocarbon interior. Also, when we compared the form factor from our X-ray data to the form factor from the MD simulations (**Fig. 4**, main paper), we find poor agreement, suggesting that the interior position of Tat is an artifact of the SDP model fitting program. This interior location of Tat, obtained using the SDP model fitting program, was the impetus for placing Tat in the interior in the MD simulation, but we discovered in **Fig.4** (main paper) that the simulation does not support this result. We show it here merely for interest.

4. Circular dichroism (CD) spectroscopy

CD spectroscopy was used to determine the secondary structure of Tat in a fully hydrated lipid environment compared to that solubilized in water. Two cuvette orientations, vertical and inverted, were used to sample different parts of the hydrated film. 8–10 scans were collected with a Jasco 715 on each sample from 260 to 185 nm at 100 nm/minute and averaged. CD data in mean residue ellipiticity were analyzed using the CDSSTR or Continll function in DichroWEB [1] with Basis Set #4 and #SP175 [2]. Uncertainties shown in **Table 1** in the main paper were estimated by averaging multiple fits to the data and taking the average and standard deviation. Precise protein concentrations of the oriented samples were determined using the absorption output of the Jasco, converting to molarity using the WEBsite http://spin.niddk.nih.gov/clore [3]. We also attempted to use the more conventional method of incorporating Tat into small unilamellar vesicles, but this was not successful, since the SUVs were unstable. We therefore used another peptide, a-synuclein (aS) with both the small unilamellar vesicle method and our thin film method and determined that both methods agreed to within 15% for the helical content. In addition, we measured the CD of Tat suspended in 3 ml water (0.05 mg/ml) without lipid.

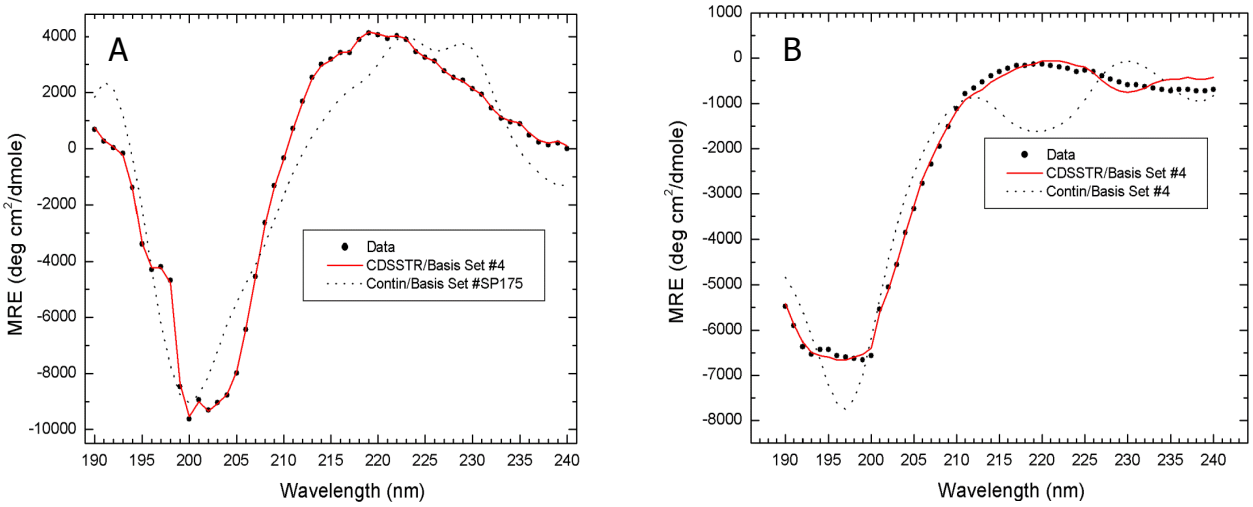

Figure S7. CD spectroscopy of **A**. Tat solubilized in water and **B**. DOPC/DOPE (3:1)/Tat, x = 0.108. Errors represent the standard deviations obtained by averaging over all algorithms and basis sets.

Fig. S7.A shows the mean residue ellipticity (MRE) vs. wavelength of Tat solubilized in water. MRE for DOPC/DOPE (3:1)/Tat, x=0.108 is shown in **Fig. S7.B.** Results of the fits to protein data sets are summarized in the Table 2 in the main paper. As shown in Table 2, there was little difference between the secondary structure of Tat solubilized in water and in an unoriented lipid film. The main 2^{o} structure in each case is β-sheet (includes regular and distorted strands and turns), followed by random coil and <10% α-helix. The random coil may also include a poly(pro)II left-handed helix (P2) [4]. These results suggest that the membrane has little effect on the 2^{o} structure of Tat, and that Tat is not an α-helix in either case.

5. Details for Fig. 9 in main paper (results from MD simulations)

Besides the results shown in the main paper in **Figs. 4, 5, 7, 9** and **Table 3**, we obtained the locations of specific atoms in the bilayer from the simulations. Using the SIMtoEXP program we grouped atoms in different ways, as shown in **Fig. S8**. ARG+ includes only the atoms in the guanidinium group for the 6 arginines in Tat, while ARG indicates the remainder of the atoms in the arginine group, including side chain carbons, alpha-carbon and adjoining peptide carbonyl and nitrogen. The two lysines were treated similarly. As shown, both the charged and uncharged parts of arginines are located closer to the bilayer center than the corresponding lysine parts. The arginines are closer to the unperturbed-by-Tat glycerol-carbonyl group (dotted line), than they are to the unperturbed phosphate groups (solid line) or to the unperturbed choline group (dashed line). However, as is shown in the cartoon in the main paper in **Fig. 9**, the perturbed phosphate groups lie closer to the bilayer center by 3.6 Å. More details of the simulation results are shown in **Table S1** which reports a weighted average based on the χ^2 of the best fit of four simulations to the X-ray data.

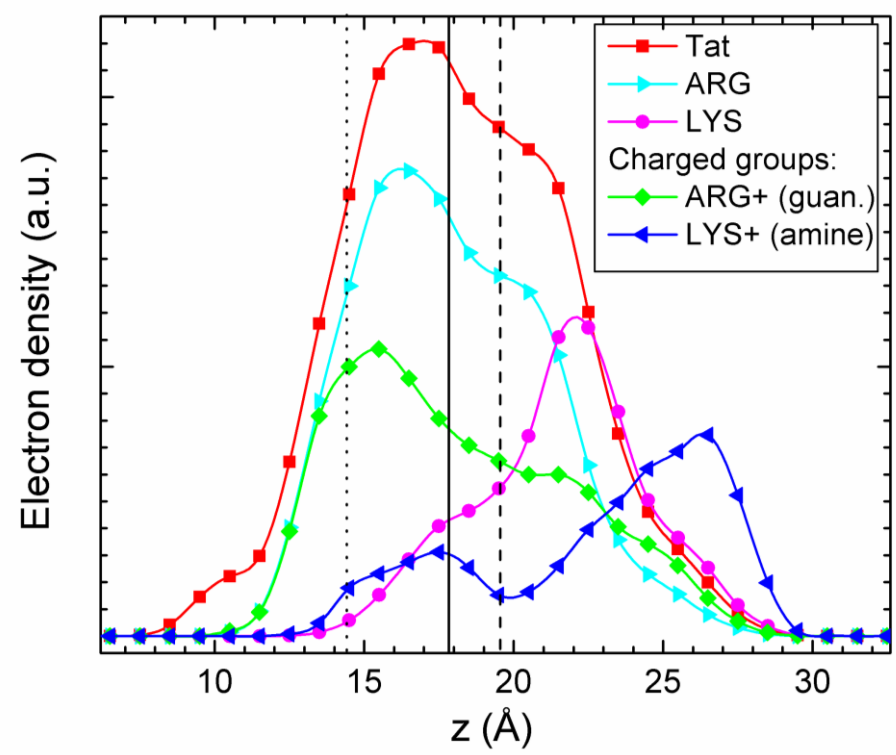

Figure S8. Distributions of components in the MD atomistic simulation of DOPC:Tat 128:2 where the area/lipid (72 Å^2) and Tat position (18 Å) agree best with our X-ray data. Tat indicates the entire Tat molecule, ARG+ indicates the guanidinium groups from 6 arginines, ARG is the rest of the arginine group, LYS+ indicates the amine groups of the 2 lysines, and LYS is the rest of the lysine molecules. The average location of the unperturbed lipid components are indicated for glycerol-carbonyl (dotted line), phosphate (solid line) and choline (dashed line).

Table S1. Results used for Fig. 9 in main paper

# of Tat	A_L	Z_{Tat}	$<D_{PP}>$	D_{PP}	x	Δt	H_{Tat}	R_{Tat}	R_2	Z_{Phos}	$Z_{guanidinium}$
2	72.9	17.1	35.4	32.7	35.6	3.6	8.7	8.3	17.1	14.6	15.1
4	75.2	17.3	34.8	31.9	NA	4.4	7.7	8.8	NA	13.8	15.4

A_L, area/lipid; Z_{Tat}, position of Tat center of mass, $<D_{PP}>$, phosphorus-phosphorus distance averaged over all lipids; D_{PP}, Tat-perturbed phosphate groups; x, = $64*<D_{PP}>-3.5*D_{PP})/60.5$ (thickness away from Tat); Δt, = $<D_{PP}^0>-D_{PP}$ (where $<D_{PP}^0>$ is the value from the pure DOPC simulation); H_{Tat}, Tat height; R_{Tat}, radius of Tat's cylinder; R_2, radius of the calculated in-plane Tat-perturbed region; R_3, effective radius of the simulation box.

6. Additional details concerning the MD simulation methods

All simulations were conducted with a 2 fs time integration step. SETTLE[5] was used to constrain water molecules and LINCS[6] was used to constrain all other bond lengths in the system. VdW interactions were truncated at 1.4 nm with a twin-range cutoff scheme and a dispersion correction was applied to both energy and pressure. Electrostatics interactions were treated with the particle-mesh Ewald (PME) method [7]. The direct term for electrostatics was evaluated within 1.0 nm cutoff and the Fourier term was evaluated with a 0.12 nm grid spacing and a 4^{th} order interpolation. Each system was simulated at 310 K using the V-rescale algorithm[8] with a 0.2 ps time coupling constant. The semi-isotropic parrinello-rahman barostat [9] was used to couple the system at 1 atm in the Z direction with a 5 ps time coupling constant, while the projected area at the X-Y plane was fixed by setting the system compressibility to 0. We inserted the Tats into the system by initially turning off all interactions between Tats and the rest of the system, with Tats constrained at different depths. Then we slowly turned on the interactions to normal strength through thermodynamics integrations. We used umbrella potentials to constrain Tats at desired depths with a force constant of 3000 KJ/mol/nm^2.

References for Supplementary data

[1] A. Lobley, L. Whitmore, B.A. Wallace, DICHROWEB: an interactive website for the analysis of protein secondary structure from circular dichroism spectra, Bioinformatics, 18 (2002) 211-212.

[2] A. Abdul-Gader, A.J. Miles, B.A. Wallace, A reference dataset for the analyses of membrane protein secondary structures and transmembrane residues using circular dichroism spectroscopy, Bioinformatics, 27 (2011) 1630-1636. DOI 10.1093/bioinformatics/btr234.

[3] N.J. Anthis, G.M. Clore, Sequence-specific determination of protein and peptide concentrations by absorbance at 205 nm, Protein Sci, 22 (2013) 851-858. Doi 10.1002/Pro.2253.

[4] N. Sreerama, R.W. Woody, Structural composition of beta(I)- and beta(II)-proteins, Protein Sci, 12 (2003) 384-388. Doi 10.1110/Ps.0235003.

[5] S. Miyamoto, P.A. Kollman, Settle - an analytical version of the shake and rattle algorithm for rigid water models, Journal of Computational Chemistry, 13 (1992) 952-962. DOI 10.1002/jcc.540130805.

[6] B. Hess, H. Bekker, H.J.C. Berendsen, J.G.E.M. Fraaije, LINCS: A linear constraint solver for molecular simulations, Journal of Computational Chemistry, 18 (1997) 1463-1472. Doi 10.1002/(Sici)1096-987x(199709)18:12<1463::Aid-Jcc4>3.0.Co;2-H.

[7] T. Darden, D. York, L. Pedersen, Particle mesh ewald - an N.log(N) method for ewald sums in large systems, J Chem Phys, 98 (1993) 10089-10092. Doi 10.1063/1.464397.
[8] G. Bussi, D. Donadio, M. Parrinello, Canonical sampling through velocity rescaling, J Chem Phys, 126 (2007) Doi 10.1063/1.2408420.

[9] M. Parrinello, A. Rahman, Polymorphic transitions in single-crystals - a new molecular-dynamics method, J Appl Phys, 52 (1981) 7182-7190. Doi 10.1063/1.328693.